Intraplaque Hemorrhage Quantification using Carotid Magnetic Resonance Imaging

Jin Liu

A dissertation

submitted in partial fulfillment of the

requirements for the degree of

Doctor of Philosophy

University of Washington

2017

Reading Committee:

Chun Yuan, Chair

William S. Kerwin

Ruikang Wang

Program Authorized to Offer Degree:

Bioengineering

University of Washington

Abstract

Intraplaque Hemorrhage Quantification using Carotid Magnetic Resonance Imaging

Jin Liu

Chair of the Supervisory Committee:
Professor Chun Yuan
Department of Radiology and Bioengineering

As a critical feature of vulnerable atherosclerotic plaque, intraplaque hemorrhage (IPH) is associated with fast plaque progression and subsequent cerebral ischemic events. Although presence/absence of intraplaque hemorrhage is a recognized biomarker for plaque vulnerability assessment, quantitative measurement of the intraplaque hemorrhage signals on MRI may contribute greater utilities to access the evolution of intraplaque hemorrhage and its vulnerability. Recent studies have demonstrated that intraplaque hemorrhage volume and signal intensity could either progress or regress along time and that the change differs between symptomatic and asymptomatic plaques. Therefore, intraplaque hemorrhage quantification may contribute to a precise assessment of atherosclerosis's

clinical risk. However, intraplaque hemorrhage detection and segmentation have mainly relied on manual review, which is not only time-consuming but also prone to measurement errors due to flexible window display level settings. Furthermore, carotid MRI often suffers from complex motion problems, causing degradation of image quality and inaccurate vessel wall delineation.

In this dissertation, a semi-automatic method was developed based on histological validation for intraplaque hemorrhage detection and quantification from magnetic resonance imaging (MRI). First, intraplaque hemorrhage detection criteria was established on the widely used Magnetization-Prepared Rapid Acquisition Gradient-Echo (MP-RAGE) sequence and recently developed Simultaneous Noncontrast Angiography and intraPlaque hemorrhage (SNAP) sequence. Both adjacent soft tissue and local median values on MP-RAGE were found to be good intensity normalization references for intraplaque hemorrhage detection, while the sternocleidomastoid muscle on the SNAP reference image was chosen for SNAP image intensity normalization. Second, a volumetric image processing method was developed on 3D SNAP and reproducibility for intraplaque hemorrhage quantitative measures were demonstrated. Lastly, a non-marker-attached motion detection and correction technique based on structured light was proposed for both abrupt and bulk motion correction in carotid MRI for better vessel wall delineation, which could also potentially improve delineation for intraplaque hemorrhage and other plaque components.

TABLE OF CONTENTS

LIST OF FIGURES

LIST OF TABLES

ACKNOWLEDGEMENTS

I would like to express my sincere gratitude to Dr. Chun Yuan for his guidance, support and inspiration. Your research passion and critical thinking will continuously affect me in my future research and career development. I feel very lucky to have you as my supervisor. Your instruction, trust and unconditional support is my continuous motivation to become a better self and make my own contribution to the work that I have passion on.

I am also indebted to Dr. William S. Kerwin, who brought me to this research field with his encouragement, trust and support. The same gratitude also goes to Dr. Jinnan Wang, Dr. Jie Sun and Dr. Niranjan Balu, for spending your precious time with me to give me guidance and support. Your genius intelligence and broad knowledge on MRI and pathology have been so inspiring to me. I cannot imagine where I would be without all your support and help. And I would also like to thank Dr. Ruikang Wang, Dr. Colin Studholme and Dr. Jenq-Neng Hwang for their valuable advice to my thesis work.

I would also like to sincerely thank Marina S. Ferguson and Vanesa Martinez-Malo, for their patients and kindness while sharing me with their remarkable knowledge in histology and pathology; and Danial S. Hippe for always been there to patiently share the rigorous and scientific statistical methods with me.

I would like to thank all the current and previous members of the Vascular Imaging Lab for their generous help, support and friendship. Special thanks go to Dr. Gador Canton, Dr. Thomas Hatsukami, Dr. Dongxiang Xu and Zachary E. Miller for their generous help and support. It feels like to be at a big family with so many talented and kind people.

Finally, my gratitude goes to my family and friends, who have always been there to support me, encourage me and accompany me to go through all ups and downs. You have made my journey so meaningful and enjoyable.

Chapter 1. INTRODUCTION

1.1 INTRAPLQUE HEMORRHAGE: A CHARACTERISTIC RISK FACTOR FOR VULNERABLE ATHEROSCLEROSIS

1.1.1 *Atherosclerosis*

Cardiovascular disease has been identified as the primary cause of death both globally [1] and in developed countries such as the United States [2] and the Europe [3]. It was estimated to cause 15.6 million deaths (29.6%) worldwide annually [1], with 0.8 million deaths (31.9%) in the United States [2] and 4 million death (46%) in the Europe [3]. Among the reasons that cause cardiovascular disease [2], atherosclerosis is the leading one [2, 4].

Atherosclerosis is an inflammatory and chronic disease occurring mainly in large and medium sized arteries [5]. The progression of atherosclerosis is a complex process mediated by many factors, with endothelial dysfunction being the first step [5]. Endothelial dysfunction increase the adhesiveness and permeability of endothelium to induce many offending agents. If the inflammatory response does not successfully remove or neutralize those agents, the inflammatory response will continue indefinitely, stimulating migration and proliferation of smooth muscle cells to form an intermediate lesion. The vessel wall is then thickened with lumen size unchanged, which is called remodeling. But continuous progression will eventually lead to focal lipid-rich necrotic core, covered by fibrous cap, forming the so-called advanced and complicated lesion [5, 6]. The occlusion and rupture of plaques can lead to ischemia of the heart, brain or extremities [5].

Although plaque stenosis is currently the main clinical criteria for plaque rupture risk evaluation, studies found that plaque rupture also frequently happens among nonstenotic plaques [7]. Recent researches have demonstrated that the components of plaque is of vital importance to determine the vulnerability of plaque rupture and future medicine treatment [4]. High risk plaques have the features of large lipid core, thin fibrous cap, intensive inflammation, increased neovasculature and/or intraplaque hemorrhage [4, 8, 9].

1.1.2 *Intraplaque Hemorrhage*

Intraplaque hemorrhage (IPH) is commonly observed in the advanced plaque lesion and was found to be a critical factor in plaque progression and destabilization [10]. The rupture of the leaky neoformed vessels within the plaque could be the source for intraplaque hemorrhage [10, 11]. The rapid accumulation of erythrocyte membrane from intraplaque hemorrhage derives free cholesterol crystals and is accompanied by macrophage infiltration, which further contribute to necrotic core volume and stimulate plaque progression [10]. The oxidant activities associated with large amounts of haemoglobin released by erythrocytes and blood-borne proteolytic activities during the evolution of intraplaque hemorrhage are also involved with the biological progress of atherosclerosis [12].

Previous research has found that carotid plaques with intraplaque hemorrhage presented were more likely to have enlarged wall volume and lipid-rich necrotic core volume and were more likely to have repeated hemorrhage [13]. Also, presence of intraplaque hemorrhage was found to have association with subsequent ischemic cerebrovascular events [14, 15] and increased risk of

plaque rupture [16]. Presence of intraplaque hemorrhage detected by magnetic resonance imaging (MRI) has been shown to be predictive of future ischemic events in both previously asymptomatic [13] and symptomatic patients [17]. Therefore, intraplaque hemorrhage detection is very important and valuable to access the vulnerability of the plaque and to predict the progress of atherosclerosis.

1.2 Non-invasive Intraplaque Hemorrhage Imaging

1.2.1 *Magnetic Resonance Imaging of Intraplaque Hemorrhage*

Atherosclerotic plaque could have very complex plaque components mixed with intraplaque hemorrhage in a relatively small region, such as calcification [18], neovasculature, macrophages and lipid-rich necrotic core [16]. With limited soft tissue contrast, computed tomography (CT) is not capable of differentiate intraplaque hemorrhage from lipid-rich necrotic core and connective tissue, although it is a time-efficient imaging modality for angiography, calcification and intracranial hemorrhage imaging [19, 20]. Similarly, ultrasound imaging cannot differentiate intraplaque hemorrhage from atheromatous debris [21]. ^{18}F-fluorodeoxyglucose (FDG)-Positron emission tomography (PET) is widely used clinically to track glucose uptake associated with disease such as cancer and inflammation. However, our previous work shown that intraplaque hemorrhage don't have enhanced FDG uptake and thus FDG-PET is not suitable for intraplaque hemorrhage detection [22].

Among these non-invasive clinical imaging modalities, Magnetic resonance imaging (MRI) is the only one that is capable of imaging intraplaque hemorrhage by identifying paramagnetic

substances such as methemoglobin [23], an oxidation product of hemoglobin, due to its T1 shortening effect. Therefore, intraplaque hemorrhage can be detected by heavily T1-weighted MRI sequences as hyperintense signals within plaque wall area [24, 25]. For example, Yuan et al. has demonstrated that high-resolution multispectral carotid MRI is capable of detecting lipid-rich necrotic core and intraplaque hemorrhage with good accuracy at 1.5-T [26], where intraplaque hemorrhage showed hyperintensity on 3D time-of-flight (TOF) images and isointensity to hyperintensity on double inversion recovery T1-weighted 2D fast spin-echo sequence.

1.2.2 *MR sequences for Carotid Intraplaque Hemorrhage Detection*

Heavily T1-weighted Magnetization-Prepared Rapid Acquisition Gradient-Echo (MP-RAGE) sequence was developed for short-T1 species imaging at 1.5-T with the advantage of good tissue contrast, high spatial resolution and short scan time [27, 28]. It has been demonstrated of good sensitivity and specificity for complicated plaque (Type VI) detection [24], where intraplaque hemorrhage can be identified as hyperintense regions compared to surrounding tissues [25, 29, 30]. With the widely use of 3.0-T MRI scanners in clinical examinations, the sequence was further optimized at 3.0-T for intraplaque hemorrhage detection by Zhu et al [25]. Comparison of the carotid intraplaque hemorrhage diagnostic performance among three T1-weighted sequences at 3.0-T and demonstrated that the optimized MP-RAGE sequence outperformed T1-weighted fast spin-echo and TOF sequences in sensitivity and specificity [30].

Although MP-RAGE has good intraplaque hemorrhage detection performance [24, 30], it was reported to suffer from flow artifact with limited blood suppression [31]. Recently, a new

sequence, named Simultaneous Noncontrast Angiography and intraPlaque hemorrhage (SNAP), has been developed to concurrently increase IPH-to-wall contrast and improve flow-suppression efficiency (Figure 1-1) [32]. Since SNAP sequence takes the advantage of an improved dynamic range offered by phase-sensitive reconstruction: in theory, it may offer higher sensitivity to intraplaque hemorrhage among existing techniques.

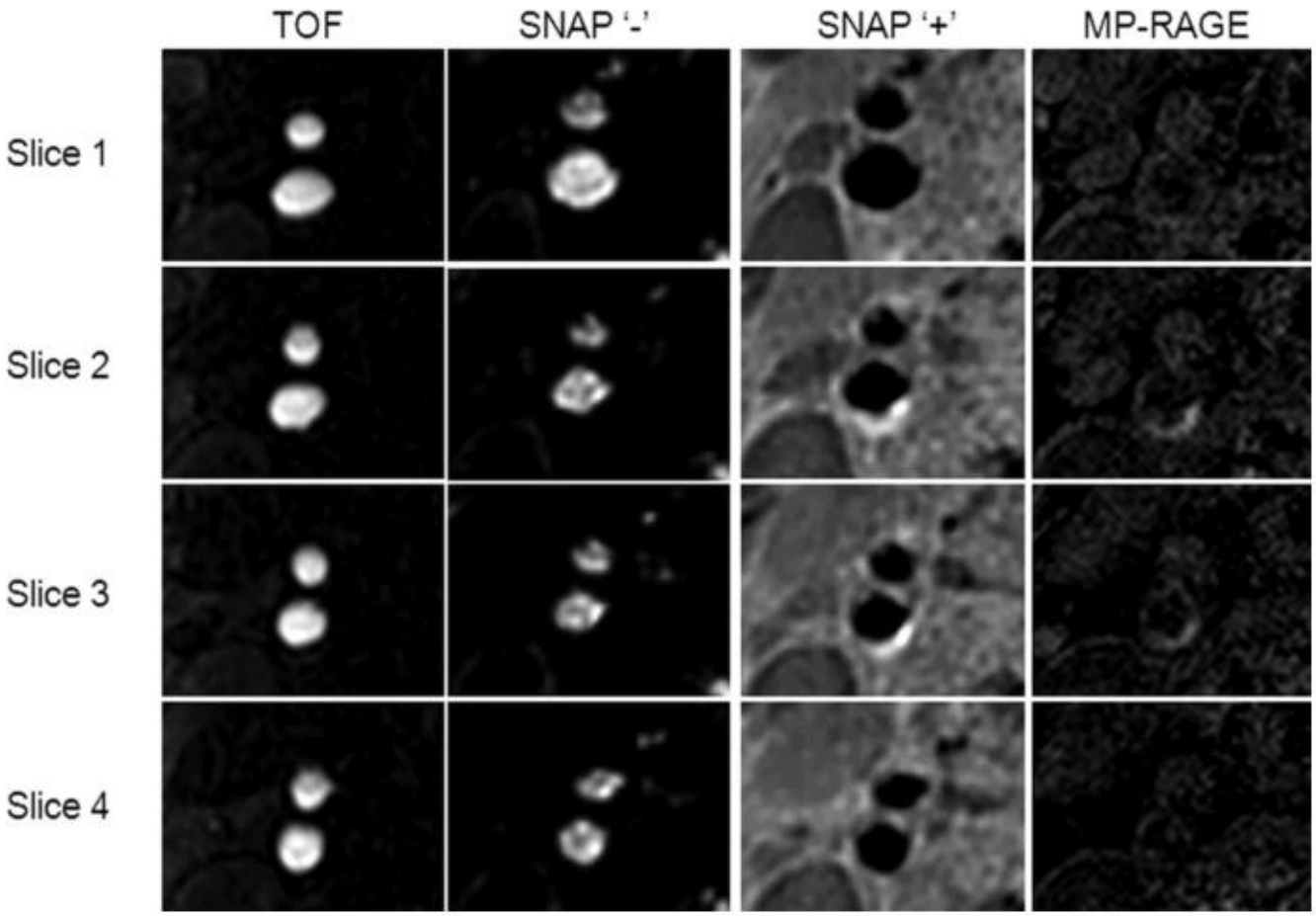

Figure 1-1. SNAP MRI can image angiography and intraplaque hemorrhage simultaneously. The angiography was comparable with TOF while the intraplaque hemorrhage detection had good agreement with MP-RAGE with higher IPH-to-wall contrast and better blood suppression compared with MP-RAEG.

1.2.3 *Challenges in Intraplaque Hemorrhage Detection*

In most MRI studies, hemorrhage was identified by manually outlining high intensity regions, as compared to fibrous tissue in the artery wall or surrounding muscle [25, 30, 32]. However, manual intraplaque hemorrhage identification may suffer from poor inter-reader reproducibility with subjective criteria. Previous study has also found that small intraplaque hemorrhages or heavily calcified hemorrhages would highly impact the intraplaque hemorrhage diagnostic performance [30], which is hard to detect by human eyes with relatively lower signal intensity compared with large and non-calcified intraplaque hemorrhage. Several studies [30, 33] have used histology as the ground truth to identify regions of intraplaque hemorrhage (Table 1-1). But no intraplaque hemorrhage detection criteria was specifically optimized using histology in those studies.

To our knowledge, studies to determine the optimum objective criteria for intraplaque hemorrhage detection in both MP-RAGE and SNAP with histology validation are lacking. Identification of an MP-RAGE hyperintensity threshold that corresponds to intraplaque hemorrhage areas verified on histology and which will ultimately allow automatic techniques for intraplaque hemorrhage detection and quantification is needed [34]. SNAP was demonstrated of good agreement with MP-RAGE for intraplaque hemorrhage detection performance ($\kappa = 0.82$) [32]. However, a full validation of SNAP with histology is still needed before full clinical adoption. And an optimized intraplaque hemorrhage detection criteria is needed for semi-automatic image review in SNAP with high reproducibility.

For semi-automatic/automatic intraplaque hemorrhage detection, signal normalization is very important before performing further analysis to get a standard signal intensity range [35].

Furthermore, carotid MRI scans use surface coils which have inhomogeneous coil sensitivity, causing extra challenges for signal normalization without pre-scan coil sensitivity correction.

Table 1-1. Previous studies that identified IPH (or high signal intensity) using MP-RAGE

Study	No of subjects	Histology	Threshold	Reference tissue	Field Intensity (T)	Coil	MPRAGE parameters, ms (TR/ TI)	Comments
Yamada et al.[36]	222	No	200%	Adjacent muscle	1.5	Standard neck array and spine array coil	1500/ 660	Define high signal intensity regions
Hishikawa et al.[33]	35	Yes	200%	Adjacent muscle	1.5	Standard neck array and spine array coil	1500/ 660	Define high signal intensity regions
Altaf et al.[17]	64	No	150%	Adjacent SCM	1.5	Receive-only quadrature neck array cervical spine coil	10.3/ 20	Define regions for IPH
Mendes et al.[37]	35	No	150%	Adjacent SCM	3	Custom designed 4 or 16 element phased array surface coils	667/ 370	Define regions for potential IPH
Ota et al.[30]	20	Yes	Subjective	Fibrous tissue and/ or adjacent muscle	3	Four-channel phased-array surface coil	13.2/ 304	Manually define regions for IPH

Note: IPH = intraplaque hemorrhage; MP-RAGE = Magnetization-Prepared Rapid Acquisition Gradient-Echo; SCM = sternocleidomastoid muscle

1.3 Carotid Intraplaque Hemorrhage Quantification in MRI

1.3.1 *Intraplaque Hemorrhage Signal Change over Time*

The status of intraplaque hemorrhage presence or absence appears to be a relatively stable biomarker that rarely changes in a few years [13, 36, 38]. Nonetheless, studies that quantitatively measured the extent or strength of intraplaque hemorrhage signals on MRI revealed that

intraplaque hemorrhage may be a highly dynamic pathological process [13, 38-40]. For example, Simpson et al. measured intraplaque hemorrhage signal intensity ratio against muscle intensity and found 16 out of 28 (57%) intraplaque hemorrhage positive plaques had detectable signal intensity ratio change during a 2-year period, although intraplaque hemorrhage presence/absence stage remained unchanged in 47/54 plaques (87%), using MP-RAGE protocol [38]. A more recent study found both visual progression and regression of intraplaque hemorrhage volume occurs in asymptomatic patients over 17-month, although quantitatively intraplaque hemorrhage volume decreased [40].

It is worth noting that although intracranial hemorrhage was found to have clear changing MR signals patterns with hemorrhage changing from hyperacute, acute, early subacute, late subacute to chronic [20], intraplaque hemorrhage differs vastly from intracranial hemorrhage due to its complexity and substrate matrix [29]. Both progression and regression of hemorrhage at different rate could happen due to surrounding degrading enzymes and/or inflammatory cells.

1.3.2 *Intraplaque Hemorrhage Quantitative Measures Correlate with Symptoms*

In recently symptomatic patients with bilateral intraplaque hemorrhage, the ipsilateral plaques showed higher T1 signals than the contralateral plaques [41]. Another 18-month longitudinal study found descending signal intensity in asymptomatic intraplaque hemorrhage, but not in symptomatic intraplaque hemorrhage, which may indicate that repeated hemorrhage is more common in symptomatic carotid plaques.

Therefore, quantitative measures of intraplaque hemorrhage signals by MRI may contribute to a more precise assessment of clinical risk beyond the mere presence of intraplaque hemorrhage and facilitate serial studies that eventually expand our knowledge on the risk factors and effective therapies of intraplaque hemorrhage.

1.3.3 *Challenges in Intraplaque Hemorrhage Quantification*

With large-coverage, three-dimensional MRI has been increasingly adopted in clinical and population studies on intraplaque hemorrhage [42, 43], there remains a lack of time-efficient method to obtain quantitative, reproducible measures of intraplaque hemorrhage signals. Previous studies largely relied on manual review of cross-sectional images [38, 41]. Manual segmentation is not only time-consuming but also prone to measurement errors due to the irregular and inconspicuous boundaries of intraplaque hemorrhage areas, which tend to change by varying window level settings.

Another gap in intraplaque hemorrhage-related research is that there are limited data on scan-rescan reproducibility of intraplaque hemorrhage signals on MRI. In part, this may be attributable to the aforementioned challenges associated with manual review. Furthermore, most reproducibility studies did not include a sufficient number of intraplaque hemorrhage plaques [44-46], prohibiting assessment of quantitative measures. Finally, the biological stability of intraplaque hemorrhage signals on MRI remains unknown. Reproducibility studies typically scan subjects twice within one month [44]. Although the presence of high T1 signals was noted to be persistent in previous studies, quantitative measures may change more rapidly with time.

SNAP MRI was developed with inversion-recovery prepared phase-sensitive acquisition to detect intraplaque hemorrhage and luminal stenosis concurrently [32]. SNAP shows flowing blood as strong negative signal, which can be exploited to generate angiograms using minimum intensity projection. With strong positive signal on SNAP, intraplaque hemorrhage is shown as hotspots in the vicinity of carotid arteries, which can be overlaid onto SNAP angiograms with intrinsic coregistration. Therefore, SNAP MRI may allow time-efficient volumetric image analysis. Improved IPH-to-wall contrast in SNAP as compared to traditional magnitude-only images may improve reproducibility of MR quantification of intraplaque hemorrhage [32].

1.4 Motion in Magnetic Resonance Imaging

Since the diagnosis of atherosclerosis components, including intraplaque hemorrhage, depending on high-resolution MRI, the image quality of MR images could highly impact the clinical assessment of the plaque [47]. However, with the relatively long duration of MR scan, patient motion often present challenge for artifact-free images, which further cause difficulty in disease diagnosis or revenue loss with rescans [48]. Patient motion during MR scan can cause blurring and ghost artifacts in MR images [49], which can affect the image quality and increase difficulty for disease diagnosis. Nearly 7.5-29.4% clinical MRI scans were found to have significant motion artifacts. The revenue lost was estimated at approximately $115,000 per scanner per year [48].

1.4.1 *Motion in Carotid MRI*

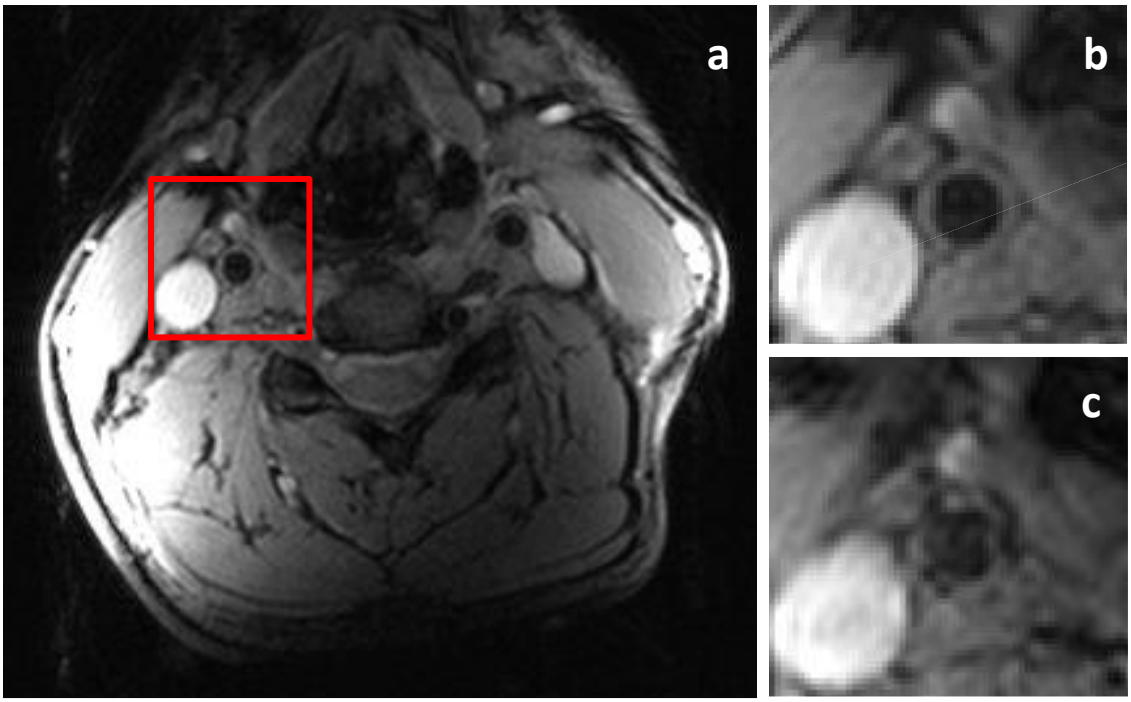

Figure 1-2. Motion artifact highly impact carotid artery wall delineation. Without voluntary motion, carotid artery wall of a healthy volunteer has smooth boundary with uniform thickness (a). The right common carotid artery area (read square) is zoomed in and shown in b; with voluntary motion (both abrupt motion and bulk motion), carotid artery wall of the same subject was hard to delineate reliably (c).

Neck motion has one of the most complex motion pattern. Beside the periodic breathing and pulsation, there could be cough, swallowing, chowing, speaking and bulk motion in the neck area. Based on a study to quantify motion in carotid artery imaging, swallow motion amplitude was 4.7 $\pm$ 2.4 mm [50]. Considering that the normal vessel wall thickness is very thin (0.5 $\pm$ 0.1 mm) [51] and the size of plaque components are also in millimeter scale, the neck motion is a big challenge for carotid MR image quality (Figure 1-2). In a previous carotid plaque research, 24 out of 160 MRI images (15%) were rejected due to motion-induced unacceptable image quality [47].

Therefore, motion correction for carotid artery MRI is very important for carotid atherosclerosis diagnosis.

1.4.2 *Motion and Intraplaque Hemorrhage*

intraplaque hemorrhage is associated with rapid plaque progression and plaque vulnerability. A small intraplaque hemorrhage could progress into a big one due to repeated hemorrhage [13]. Therefore, detection of small intraplaque hemorrhage is very important to diagnose risky plaques at early stage, enabling early control of fast-progressing plaques with aggressive medical treatment.

However, the detection of intraplaque hemorrhage, especially small one, can be missed in MR images when there are motion artifacts. Although SNAP and MP-RAGE sequences were optimized for intraplaque hemorrhage detection [25, 32], they were found to have low sensitivity for small intraplaque hemorrhage [30]. For example, in our previous study on SNAP with resolution of 0.64 mm^2, the sensitivity for intraplaque hemorrhage with area bigger than 0.64 mm^2 and smaller than 4.52 mm^2 was only 31%. By studying the cases with small intraplaque hemorrhage in histology but no hyperintensity signal in matched SNAP slices, we found that nearly half of these cases had poor image quality mainly due to motion problems. Therefore, motion correction for carotid MRI is critical for improving intraplaque hemorrhage detection sensitivity, as well as delineating other structures in carotid plaque.

1.4.3 *Current Motion Correction Methods*

There have been many techniques proposed for motion detection and correction in MRI, which can be divided based on mediation occurring time into prospective and retrospective motion correction [52]; or based on motion detection methods into three kinds: navigator based, self-navigation and external device based motion correction. In the following, current motion correction methods are discussed with the focus on the technique applicable to carotid MRI.

Prospective motion correction is a technique capable of updating pulse sequence during the acquisition based on detected motion information [52]. When rotation or translation information are measured, motion can be compensated by rotating gradient waveforms, changing slice select center frequency or re-acquiring motion corrupted data. In this way, motion is minimized or compensated before causing artifacts in the reconstructed images. However, prospective motion correction may require extra scanning time for motion measurement or re-acquiring. The other category is retrospective motion correction, where data is corrected after acquisition based on measured motion or iterative correction to maximize data consistency. Retrospective motion correction may not increase scan time but may require more sophisticated algorithms during image reconstruction.

Navigator-based motion correction has been developed and applied on swallowing detection in carotid MRI [53, 54]. In Crowe et al.'s research [54], a crossed pair navigator was placed on the epiglottis to track swallowing motion. A $\pm$ 2 mm acceptance window was used for prospective gating. However, the navigator placement need to be carefully adjusted to avoid carotid artery area, as well as capture the motion of epiglottis. Furthermore, carotid MR scans often use surface

coil with low signal-to-noise ratio (SNR) in the deep epiglottis region, making epiglottis monitoring more challenging.

Another newly proposed free-induction decay (FID) navigator gating may overcome the above limitations [55]. FID navigators monitor the center of k-space, which is sensitive to motion in all directions. Since it was implemented in a stand-alone module, this technique can be applied to any sequence. FID navigator gating have demonstrated effective image quality improvement in healthy volunteer scanning who were instructed to swallow or breathe deeply. However, this technique cannot handle the situation when bulk motion occurs, which could cause drifting of signal and thus change the baseline level.

Another alternative for swallowing detection is self-gating technique [56]. In Fan et al.'s work, self-gating signal along the superior-inferior direction was acquired to derive the projection profile which was compared with reference profile using cross-correlation for swallowing motion detection. This technique has been applied on both healthy volunteers and atherosclerosis patients. Improved vessel wall and plaque components delineation were achieved with self-gating. However, this technique suffers the same problem as the FID navigator when bulk motion happens.

Some external devices have been developed to monitor swallowing motion in the neck area [57, 58]. For example, an external magnetic coil was placed on the surface of the neck to track swallowing motion in Chan's research [57]. Effective motion artifacts removal was obtained in healthy volunteers. But these kinds of technique require devices to be attached on the patients,

which is subject to shift and can cause discomfort for patients. Breath belts, the most popular external device based motion detection techniques for breathing motion, may suffer from drifting and cannot provide accurate absolute motion measurement [59]. Recently, optical marker-tracking technique [52] has been proved to be capable of measuring the exact motion of rigid imaging targets, usually head, to improve the image quality. But neck motion is mainly non-rigid and thus is hard for those markers to correct.

There are also post-processing motion correction methods available base only on acquired MR data [60]. For example, Huang et al proposed a retrospective motion correction method by data convolution and combination and demonstrated its effectiveness in reducing ghost artifacts caused by swallowing, breathing or blood flow. Although it has the advantage that no motion detection device or sequence is needed, post-processing motion correction often involve complex algorithm and is computationally expensive. Furthermore, it may fail when motion is complex without any prior motion information.

1.4.4 *Challenges in Motion Correction of Carotid MRI*

As discussed above, navigator based methods or self-gating usually need extra time with sequence dependency; current external devices need markers or coils to be attached on patient surface, causing discomfort to the patient, which is also not practical due to the limited neck space with carotid coils already attached. More importantly, current motion correction techniques have only showed efficiency on motion like swallowing and would easily fail when bulk shift motion happens. Therefore, for carotid MRI which is inherently susceptible to complex motion, a more

robust motion correction technique capable of correcting both abrupt motion and bulk motion is needed, without sacrificing scanning time or attaching devices on patients.

Structured light has been used for depth measurement with high accuracy without contact with the object [61]. Previous study has used structured light to track the head motion in the PET scanner and demonstrated good accuracy and stability [62]. Another study demonstrated the feasibility and accuracy of using structured light for motion tracking in an MR head coil [63]. However, their experiments were performed outside of the MR scanner due to both geometry and MR-compatibility limitation. Two cameras were used instead of one, which further added geometry limitation to their system. Study using structured light for motion detection and correction during MRI scans is limited.

1.5 Research Goal and Hypothesis of This Study

As discussed in the above sections, intraplaque hemorrhage is a critical factor in atherosclerosis progression. The detection and quantification of intraplaque hemorrhage may contribute to assessing the rupture risk of plaque and facilitate the pursuit of targeted therapies. However, there remains a lack of time-efficient and histology-validated method to obtain intraplaque hemorrhage detection and quantification measures. Furthermore, complex neck motion highly impacts the delineation of carotid vessel wall and plaque components, yet the current motion correction methods for carotid MRI still face many challenges and are hard to be adopted in clinical use. To fill these gaps, the research goal of this study is to develop a semi-automatic carotid

intraplaque hemorrhage detection and quantification method in carotid MRI with novel motion correction technique.

We hypothesize that semi-automatic carotid intraplaque hemorrhage detection and quantification on MRI have good intraplaque hemorrhage detection performance and reproducible intraplaque hemorrhage quantification measurements and that motion detection and correction of carotid MR image can further improve the carotid vessel wall visualization for future intraplaque hemorrhage quantification.

To test the hypothesis, the following studies are proposed.

Specific Aim I: To establish intraplaque hemorrhage detection criteria on MRI and evaluate its intraplaque hemorrhage detection performance.

a) Obtain intraplaque hemorrhage detection criteria in MP-RAGE MRI.
b) Obtain intraplaque hemorrhage detection criteria in SNAP MRI.
c) Evaluate the intraplaque hemorrhage detection performance of MP-RAGE and SNAP MRI

Specific Aim II: To develop a semi-automatic method for quantitative intraplaque hemorrhage measurement and evaluate its reproducibility.

a) Develop a semi-automatic method for quantitative intraplaque hemorrhage measurement.
b) Evaluate the reproducibility of intraplaque hemorrhage quantification measures.

Specific Aim III: To develop a motion tracking and correction technique using structured light to improve carotid artery wall delineation.

a) Develop a motion tracking system using structured light.
b) Detect both abrupt motion (such as cough and swallowing) and bulk motion during MR scans.
c) Correct both abrupt carotid motion and bulk motion in carotid MRI.

Overall, intraplaque hemorrhage detection criterial will be established using histology as the gold standard and a semi-automatic and reproducible volumetric image processing method will be developed for quantitative intraplaque hemorrhage characterization. A novel motion correction technique with both abrupt and bulk motion correction capability will be developed for carotid atherosclerosis MR imaging to improve the carotid artery vessel wall delineation with the merits of no attaching to patients and independence of MR sequence.

Chapter 2. INTRAPLAQUE HEMORRHAGE DETECTION IN CAROTID MRI

2.1 OVERVIEW

As discussed in Chapter 1, the presence of intraplaque hemorrhage (IPH) is an important indicator for plaque vulnerability and future clinical events. However, current intraplaque hemorrhage detection have been relaying on subjective evaluation by human reviewers or arbitrary unverified intensity threshold. Therefore, the research goal of this study was to replace those subjective evaluations with objective threshold for intraplaque hemorrhage detection on both MP-RAGE and SNAP MRI and evaluate their intraplaque hemorrhage detection performance.

In order to accomplish this goal, the following studies were performed: 1) the intraplaque hemorrhage intensity thresholds were optimized in MP-RAGE and SNAP using histology specimen as the gold standard; 2) the sensitivity and specificity of intraplaque hemorrhage detection on MRI were calculated using the optimized thresholds.

2.2 INTRAPLAQUE HEMORRHAGE DETECTION IN HISTOLOGY

2.2.1 *Histology Specimen Processing*

In order to have histology specimen as the intraplaque hemorrhage detection gold standard, carotid endarterectomy (CEA) patients were recruited for this study. Patients with either asymptomatic, greater than 80% carotid artery stenosis or symptomatic, greater than 70% carotid artery stenosis were recommended for CEA surgery [30] to prevent future stroke. Before the

surgery, patients underwent MR scans including MP-RAGE and/or SNAP, as well as conventional MR sequences (T1-weighted, T2-weighted and TOF).

Processing and analysis of CEA specimens were consistent with previous studies [30, 64, 65]. During the CEA surgery, carotid plaque was removed with an effort to keep its structure intact. Within 4 hours following the CEA, carotid plaque specimens were fixed in 10% neutral buffered formalin. They were then decalcified in 10% formic acid, embedded in paraffin and sectioned at every 1.0 mm in the common carotid and at every 0.5 mm in the internal carotid (Figure 2-1). The sections (10 μm) were stained with hematoxylin-eosin [30].

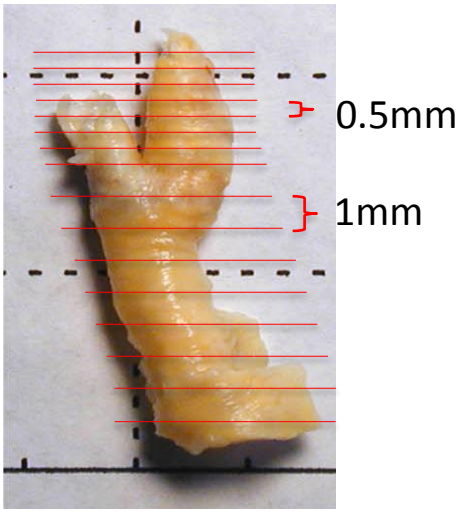

Figure 2-1. Carotid plaque removed by carotid endarterectomy for histology processing. Red lines represent the sectioning positions (every 0.5 mm in the internal carotid artery and every 1 cm in the common carotid artery).

2.2.2 *Intraplaque Hemorrhage Delineation in Histology*

By carefully checking the hematoxylin-eosion stained histology sections under microscope, an experienced histologist, blinded to MRI results, outlined intraplaque hemorrhage boundaries [30] on each section photo if there was any intraplaque hemorrhage identified (MATLAB). The

presence/ absence of intraplaque hemorrhage for each section was recorded. And the area of intraplaque hemorrhage for each section was measured and recorded with photo size calibrated.

2.2.3 *Matching between histology and MRI*

In order to be blinded to MP-RAGE and SNAP findings, only conventional MR images (co-registered T1-weighted, TOF and T2-weighted images) were used to match with histology sections. The matching was also performed independently from the histology measurements.

Due to the slice thickness and gap difference between conventional MR axial image (2 mm thickness at every 2 mm) and histology sections (10 μm thickness at every 1 mm or 0.5 mm), multiple histology sections could be matched to the same MR location. The averaged area of intraplaque hemorrhage among matched histology sections was calculated for each MR location. Other matching challenges include the imperfect match of slice direction between histology and MRI, as well as the shrinkage of histology specimen. Therefore, not only the bifurcation level but also plaque morphology and components (e.g. calcification) morphology information were used to facilitate the matching between histology and MRI.

2.3 MR IMAGE PRE-PROCESSING

Image intensity normalization is an important pre-processing step in analyzing MR images, because MR image signals have a variety of intensity range, even at different time points from the same scanner with the same MR sequence [35]. In carotid plaque MRI, adjacent muscle such as sternocleidomastoid muscle, and fibrous tissue which is considered as the normal artery wall

tissue inside carotid artery, were often used as the intensity reference to normalize the MR image signal intensity [34, 66]. This is also in accordance with the human reviewers who define hyperintensity and hypointensity of the artery wall by comparing it with adjacent SCM and/or normal artery tissue [26].

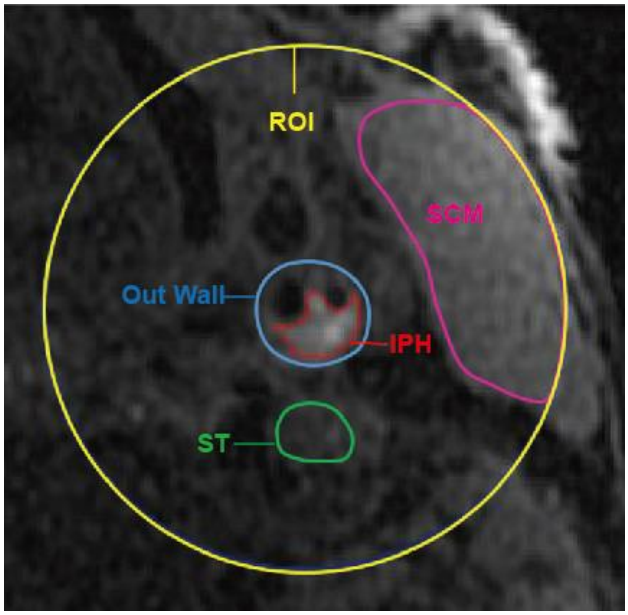

Figure 2-2. MP-RAGE image slice with lumen, out wall, reference and ROI contours. ROI is centered at the carotid artery with a radius of 2 centimeters (yellow circle). SCM = sternocleidomastoid muscle; ST = adjacent soft tissue; IPH = intraplaque hemorrhage.

2.3.1 *MP-RAGE Image Intensity Normalization*

Since original pixel value in MP-RAGE images varies not only between patients, but also between axial slices due to the inhomogeneous coil sensitivity, original pixel value should be normalized by dividing the signal intensity of a reference region. The choice of a reference to calculate the threshold can also affect diagnostic performance. Therefore, three types of signal intensity references were selected. Two references required manual outlining: the mean value of the sternocleidomastoid muscle (SCM) within the ROI and the mean value of adjacent soft tissue (ST) drawn as a small region adjacent to the carotid artery that visually appears of similar intensity

compared with presumed dense fibrous tissue within the non-plaque portion of the carotid artery wall. The third reference was the median signal intensity value (MED) within ROI [67]. The adjacent soft tissue reference was chosen beside the sternocleidomastoid muscle because the muscle is closer to the skin surface and may be biased towards a higher value relative to the carotid artery due to the surface coil sensitivity. Ratios of the signal intensity of each pixel within the vessel wall and signal intensity of each reference (SCM, ST or MED) within the same slice were calculated to produce relative values more comparable between slices and subjects.

2.3.2 *Coil Sensitivity Normalization in MP-RAGE*

Due to the inhomogeneous coil sensitivity, the intraplaque hemorrhage detection in MP-RAGE may be affected by the coil sensitivity with the varying depths of carotid artery from the skin with different intensity level. Previously, Han et al proposed a coil correction method based on wavelet transform [68] and showed promising results in images of both phantom and human images, without using any prior knowledge of the subject or coil. In order to access the effect of coil sensitivity, coil sensitivity correction [68] was applied on MP-RAGE images before threshold optimization. The intensity of SCM, adjacent soft tissue and local median value before and after coil correction were compared.

2.3.3 *SNAP Image Reformation and Signal Intensity Normalization*

Since the optimized intraplaque hemorrhage intensity threshold on SNAP images would be applied directly on 3D SNAP images in the next step, during the intensity optimization, 3D SNAP images were reformatted to 0.4 mm thick 2D axial slices in consistence with 3D SNAP images.

SNAP utilizes phase-sensitive inversion recovery [32, 69] and three sets of images are generated simultaneously [70]: 1) heavily T1-weighted images (I1); 2) proton density-weighted reference images (I2); and 3) phase-corrected images (SNAP). Only static tissues with short T1 are hyperintense on SNAP, making it well suited for detecting intraplaque hemorrhage. The SNAP image also shows carotid lumen as strong negative signals so its negative portion can be used for MR angiography. However, other soft tissues including commonly used sternocleidomastoid muscle (SCM) and normal vessel wall have near-zero signal intensities and are thus not suitable as reference tissues. Therefore, the signal intensity of SCM on I2, sampled by using a 2D region-of-interest (ROI) close to the common carotid bifurcation was used for signal intensity normalization. SNAP images were normalized voxel-by-voxel to the mean signal intensity of SCM on I2.

Unlike MP-RAGE, SNAP MRI has built-in coil sensitivity correction, which mitigates influences of coil sensitivity on signal intensity measurements [32]. Therefore, coil sensitivity correction was not necessary for SNAP and only a single SCM ROI was selected for each artery.

2.4 Intraplaque Hemorrhage Intensity Threshold Optimization

Receiver operating characteristic (ROC) curves for detection of intraplaque hemorrhage were generated for each of the reference methods by comparing the presence/ absence of intraplaque hemorrhage in MR images with that in matched histology slices. The overall performance was summarized using the area under the ROC curve (MATLAB, R2010b, US). The optimal threshold

was then chosen as the one with the maximum Youden's Index (sensitivity+specificity-1), which weighted sensitivity and specificity equally.

In order to eliminate the effect of co-localized calcification and resolution limits of MRI [30], sub-sets of data excluding slices with small intraplaque hemorrhage areas or calcified intraplaque hemorrhage (>50% intraplaque hemorrhage area calcified) were also analyzed. Small intraplaque hemorrhage area thresholds were set by $\pi \cdot (x \cdot \text{pixel length})^2$ with x being 1 and/or 1.5 by referring to previous established method [30]. AUCs for detecting presence/absence of intraplaque hemorrhage in MR images using various thresholds were also calculated.

2.5 In Vivo Experiment on MP-RAGE

2.5.1 *Imaging Population*

14 patients scheduled for carotid endarterectomy were recruited for this study, which was a subset of a previously reported group [30], all scanned at Michigan State University. All patients signed IRB-approved consent forms. According to the criteria for carotid endarterectomy at our institution, patients were either asymptomatic with greater than 80% carotid stenosis or symptomatic with greater than 70% carotid stenosis.

2.5.2 *MR Imaging*

Before the carotid endarterectomy surgery, patients were imaged on a 3T Signa HDx MR scanner (GE Healthcare, Waukesha, WI) using a dedicated 4-channel carotid bilateral phased-array coils

(Pathway MRI, Seattle, WA). An optimized 3D MP-RAGE sequence [25] was used (TR/TE=13.2ms/3.2ms, in plan spatial resolution = 0.63 mm × 0.63 mm, reconstructed resolution = 0.31 mm × 0.31 mm, slice thickness = 1 mm, TI = 304 ms, acquisition time = 3 min 50 sec). Fat suppression was achieved by water selective excitation.

2.5.3 *MR Image Analysis*

Carotid lumen and outer wall boundaries were drawn by two experienced reviewers trained in carotid plaque MR image interpretation. The MR readers were blinded to the histology results. Within each image, all analysis was performed within a 4 centimeter diameter circular region of interest (ROI), centered at the carotid lumen. This ROI was chosen to reduce the effect of signal inhomogeneity associated with the surface coil while generally still including sufficiently large reference areas (Figure 2-2).

Considering the resolution limit of MRI and possible hyperintensity of heavily calcified intraplaque hemorrhage, the analysis was conducted using all slices as well as after excluding subsets of slices with heavily calcified intraplaque hemorrhage or with intraplaque hemorrhage area < 1.25 mm^2 or < 2.8 mm^2 measured on histology [30], where the area thresholds were calculated using $\pi(0.63x)^2$ with x being 1 and 1.5, respectively, and 0.63 (mm) being the resolution of MP-RAGE images.

2.5.4 *Coil Generality Test*

In order to investigate whether surface coil could make a difference on signal ratios, surface coil sensitivity correction was applied using Han et al.'s automatic multi-scale coil correction method based on the wavelet transform [68]. For each slice, signal ratios of maximum intensity within the artery over the three references (SCM, ST, MED) were calculated before and after coil correction. The bootstrap method was used to calculate confidence intervals for the signal ratio change percentage after coil correction (R, version 3.0.2, Austria).

2.5.5 *Statistical Analysis*

After intraplaque hemorrhage signal intensity optimization, the thresholds were used to measured areas of intraplaque hemorrhage on MRI and were compared with histology using Pearson's correlation coefficient (SPSS Statistics 21, US). The nonparametric bootstrap and percentile method were used to compute 95% confidence intervals [71, 72] (R version 3.0.2, Vienna, Austria).

2.5.6 *Results*

133 axial MR slices from 14 patients were matched with histology specimens, among which 63 slices had intraplaque hemorrhage identified in histology. Eight of the 133 slices were excluded when the SCM was used as reference, because the SCM in those slices were more than 2cm away from the artery, outside the primary ROI.

Table 2-1. Optimized thresholds for detecting IPH

Data subset			Area Under the ROC Curve (95% confidence interval)			Optimized threshold,% (95% confidence interval)		
	IPH Area (mm^2)[a]	n+/n[b]	SCM	ST	MED	SCM	ST	MED
With CA	>0	63/133	0.69 (0.53-0.83)	0.71 (0.55-0.86)	0.58 (0.42-0.75)	100 (73-131)	162 (115-208)	223 (197-275)
	>1.25	52/122	0.71 (0.56-0.87)	0.72 (0.56-0.84)	0.64 (0.45-0.80)	101 (83-131)	162 (129- 208)	223 (217-275)
	>2.80	34/104	0.74 (0.64-0.91)	0.79 (0.55-0.88)	0.68 (0.46-0.85)	104 (83-131)	160 (130-167)	223 (218-275)
No CA[c]	>0	49/119	0.74 (0.58-0.86)	0.71 (0.52-0.87)	0.66 (0.49-0.81)	100 (83-131)	170 (115-208)	223 (182-275)
	>1.25	40/110	0.76 (0.50-0.88)	0.71 (0.60-0.86)	0.72 (0.54-0.86)	101 (83-131)	170 (140-208)	223 (217- 275)
	>2.80	25/95	0.83 (0.71-0.91)	0.80 (0.60-0.92)	0.80 (0.66-0.91)	104 (89-131)	162 (140-208)	223 (217-275)

Note: IPH = intraplaque hemorrhage; MED = median value; ROC = Receiver operating characteristic; SCM = sternocleidomastoid muscle; ST = soft tissue.

[a] IPH area: excluding IPH with areas $< \pi (0.63x)^2$, where 0.63mm was the in-plane resolution of MP-RAGE, and x was set as 1 and 1.5 which gave areas of 1.25 and 2.80

[b] n+: number of slices with IPH present in histology; n: total number of slices

[c] No CA: excluding heavily (>50%) calcified IPH; with CA: not excluding heavily calcified IPH

Table 2-2. Performance of optimized thresholds

Data subset			Sensitivity (%)			Specificity (%)			Pearson's correlation coefficient (r)		
	IPH Area(mm^2)	n+/n	SCM	ST	MED	SCM	ST	MED	SCM	ST	MED
With CA	>0	63/133	51	46	51	81	88	80	0.62	0.84	0.81
	>1.25	52/122	57	54	60	82	87	80	0.62	0.84	0.81
	>2.80	34/104	57	68	68	84	84	80	0.64	0.85	0.81
No CA	>0	49/119	57	49	57	81	90	80	0.77	0.93	0.89
	>1.25	40/110	62	52	67	82	90	80	0.78	0.93	0.89
	>2.80	25/95	68	68	80	84	87	80	0.79	0.94	0.90

Note: IPH = intraplaque hemorrhage; MED = median value; SCM = sternocleidomastoid muscle; ST = soft tissue.

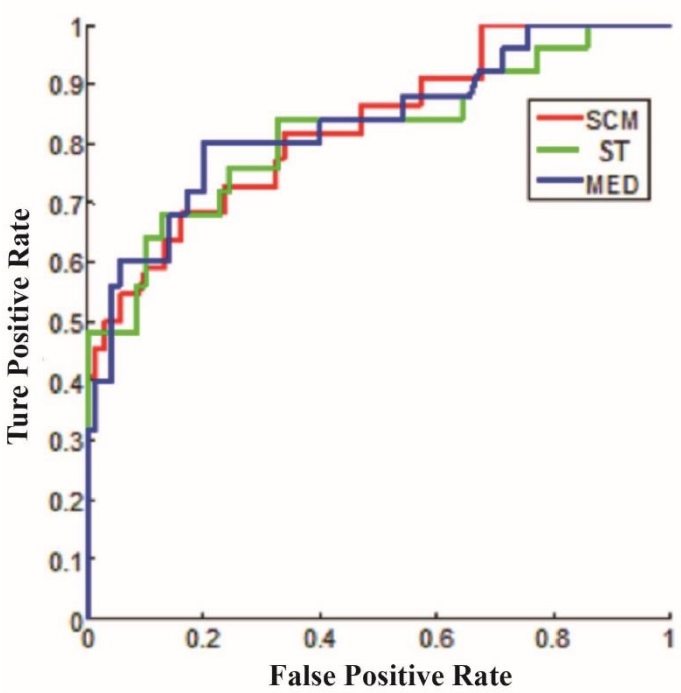

Figure 2-3. Receiver operator curves for IPH detection using three reference standards (SCM, ST and MED). The subset of slices without heavily calcified IPH or IPH <2.8 mm^2 was used.

ROC curves for the subset excluding slices with intraplaque hemorrhage area < 2.80 mm^2 or heavily calcified intraplaque hemorrhage are plotted in Figure 2-3. The area under the ROC curve for each subset is shown in Table 2-1 for all three references. When compared to the full dataset, the area under the ROC curve increased when heavily calcified intraplaque hemorrhage and intraplaque hemorrhage with areas area <2.80 mm^2 were excluded. However there were no differences observed for ROC or area under the ROC curve between different references.

Optimized thresholds to detect the presence of intraplaque hemorrhage are also summarized in Table 2-1. Using different data subsets, the optimized intraplaque hemorrhage signal intensity threshold remained about the same, being 100-104% of SCM, 160-170% of ST and 223% of MED.

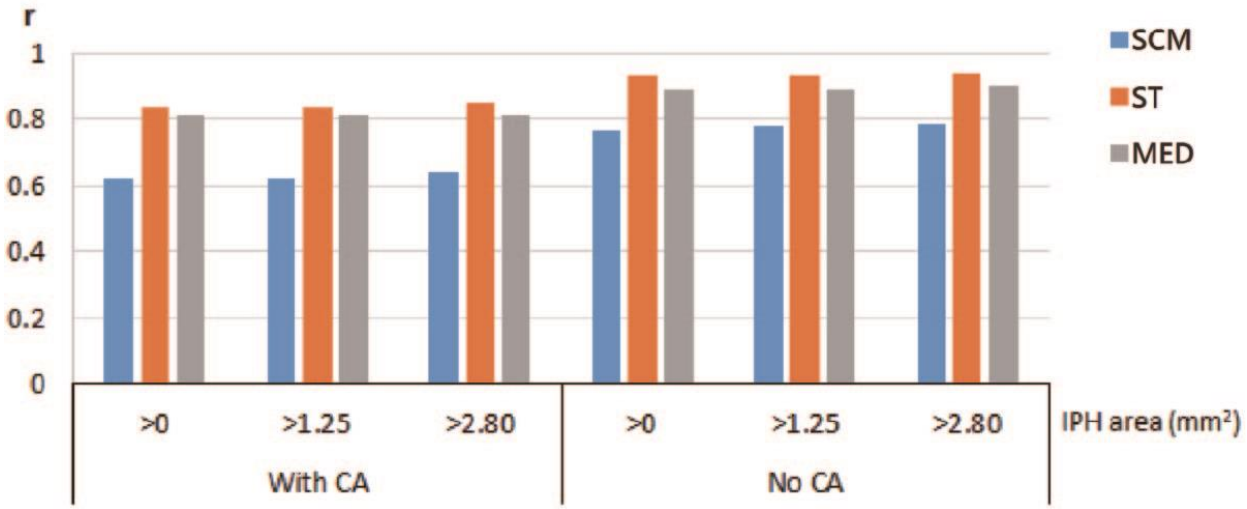

Figure 2-4. Pearson's correlation coefficients (r) of IPH area measured in MP-RAGE images and histology using optimized thresholds based on three references for different subsets of data.

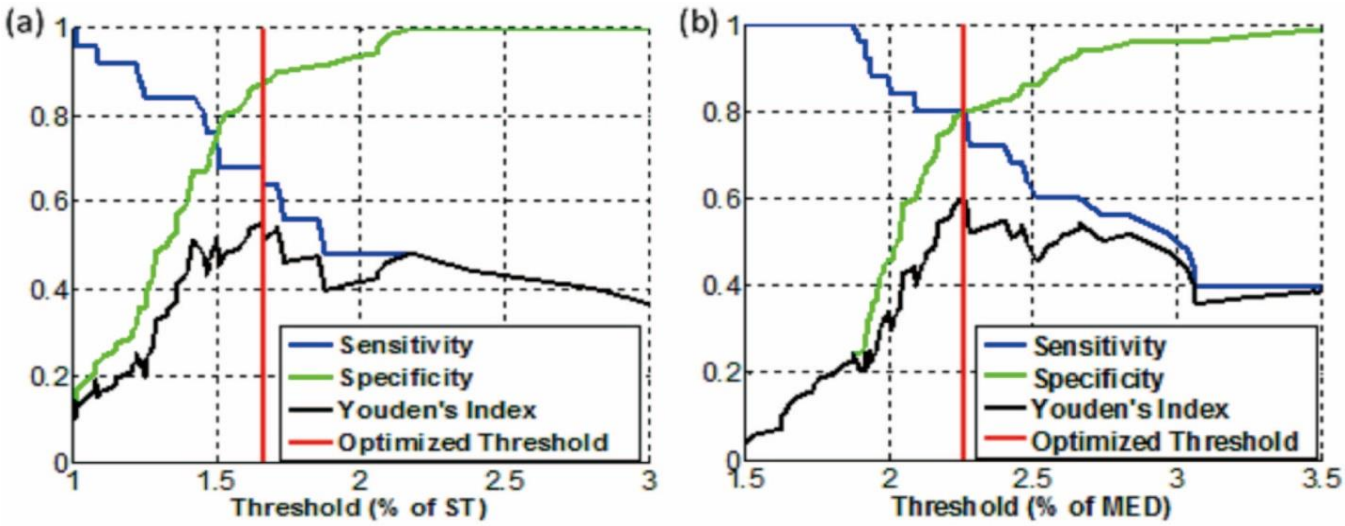

Figure 2-5. Sensitivity and specificity using different thresholds based on two types of references: (a) ST (adjacent soft tissue) and (b) MED (median value within ROI). Red line shows optimized thresholds (heavily calcified IPH areas and IPH area<2.80mm2 excluded, n=95).

The performance of optimized thresholds is summarized in Table 2-2. When heavily calcified intraplaque hemorrhage and small intraplaque hemorrhage were excluded, sensitivity increased from 51% to 68% for SCM, from 46% to 68% for ST and from 51% to 80% for MED; Pearson's correlation coefficients (r) increased from 0.62 to 0.79 for SCM, from 0.84 to 0.94 for ST and from 0.81 to 0.90 for MED (Figure 2-4). Specificity did not change with different subsets: 81%-84% for SCM, 84%-90% for ST and 80% for MED. The sensitivity, specificity and Youden's index for various thresholds using the ST and MED as reference are shown in Figure 2-5. Semi-automatic intraplaque hemorrhage identification using threshold based on MED compared well with histology identified intraplaque hemorrhage.

After surface coil sensitivity correction, signal intensity ratios of the artery to the ST and MED reference had relatively small changes compared to their values before coil correction (+5%, $p = 0.16$ and -6%, $p = 0.03$, respectively). However, the signal intensity ratio based on the SCM reference showed a much larger change after coil correction (46%, $p < 0.01$).

2.5.7 *Discussion*

By using histology as the gold standard, this study provides the optimized thresholds for three different references in the detection of carotid intraplaque hemorrhage by MP-RAGE MRI.

A threshold of 162% based on ST was found to have good performance for intraplaque hemorrhage detection with high correlation ($r = 0.84$-0.94) for intraplaque hemorrhage area. As such, the ST method is recommended for intraplaque hemorrhage detection where an adjacent,

soft tissue region that is isointense with fibrous plaque can be readily identified and manually outlined. For a more automated intraplaque hemorrhage detection method, the local median appears to be the optimal choice for efficiency and accuracy, considering that the threshold of 223% based on MED is nearly as accurate as ST with intraplaque hemorrhage area correlation r = 0.81-0.90. Of note, we found that the optimized threshold for the commonly used SCM reference method [17, 37] is around 100%, suggesting that using the sternocleidomastoid muscle as reference may be problematic without surface intensity correction when surface coils are used. Also, the measured intraplaque hemorrhage area correlation between MP-RAGE and histology is relatively low using SCM as reference compared with ST and MED (Figure 2-4).

Although surface coil was used in this study, our results demonstrated that coil correction had a relatively minor, if any impact, on signal intensity ratios based on ST or MED, suggesting that the optimized threshold based on ST or MED is also applicable with other kind of coils, such as neurovascular coils that are readily available on major scanner platforms.

Figure 2-5 provides thresholds for selection by determining the desired optimum sensitivity, specificity for the ST and MED methods. A threshold with higher sensitivity may be preferred to screen patients for intraplaque hemorrhage, whereas a threshold with a lower false positive rate may be preferable for clinical decision-making.

Some previous studies have used similar relative intensity thresholds (e.g. 150% or 200% of adjacent muscles signal) to determine hyperintensity [17, 33]. Yamada et al. [36] utilized 200% of adjacent muscle signal as threshold for “high signal intensity” in MP-RAGE images. Using the same

threshold, the same group [33] used histology as reference and found that carotid plaques with hyperintensity in MP-RAGE had large necrotic cores containing intraplaque hemorrhage. A threshold of 150% of adjacent SCM signal were also utilized in other research [17, 37] for defining intraplaque hemorrhage or potential intraplaque hemorrhage areas. In addition, Zhu et al.'s study outlined intraplaque hemorrhage ROIs in carotid MP-RAGE images, referring to matched histology specimens [25]. In four patients, intraplaque hemorrhage showed averaged signal intensity values as 227.4%, 244.1%, 322.4%, 266.2% of adjacent sternocleidomastoid muscle mean intensity.

Compared with manual intraplaque hemorrhage detection, automatic or semi-automatic intraplaque hemorrhage detection has the advantage of higher repeatability and requires less time. Ota et al. [30] manually outlined intraplaque hemorrhage for 20 patients scheduled for carotid endarterectomy using the MP-RAGE sequence and evaluated the performance by referring to histology ground truth. Our study only include a subset population of Ota et al.'s (14 out of 20) scanned from one site. Using the semi-automated MED technique, we found better intraplaque hemorrhage area correlation with histology ($r = 0.90$ compared with $r = 0.813$) and comparable sensitivity (80% compared with 80%) but lower specificity (80% compared with 97%). We assume the specificity of automatically detecting intraplaque hemorrhage can be improved by combining threshold method with information of plaque morphology [67] and/or area of hyperintensity.

Furthermore, specificity, area under the ROC curve and Pearson's correlation coefficient increased when heavily calcified intraplaque hemorrhage and/or intraplaque hemorrhage smaller than cutoff area was excluded. This is likely due to 1) co-localized calcification resulting in lowered

intraplaque hemorrhage signal intensity and 2) intraplaque hemorrhage areas smaller than the detection threshold of MP-RAGE. However, the optimal threshold was found to be stable regardless of the present/absence of these characteristics. This suggests that using these thresholds can detect intraplaque hemorrhage with the caveat that sensitivity may be reduced in populations with small or heavily calcified intraplaque hemorrhage. Furthermore, when calcification can be identified with other MRI weighting, reduced intensity threshold can be used for increasing co-localized intraplaque hemorrhage detection sensitivity.

One limitation of the current study is that the thresholds were optimized based on intraplaque hemorrhage presence/ absence information in each slice, without considering the location of detected intraplaque hemorrhage within the slice or its size. Nevertheless, based on our observation, the location of detected intraplaque hemorrhage in MP-RAGE mostly coincided with the true intraplaque hemorrhage location in histology when checked visually. While the optimized threshold was determined without consideration of size of intraplaque hemorrhage, our study demonstrates that the size of intraplaque hemorrhage detected using optimized thresholds correlates well with that in histology ($r = 0.94$ for ST and $r = 0.90$ for MED). Another limitation is that we did not assess the effect of varying MP-RAGE imaging parameters on optimized thresholds. We used MP-RAGE parameters previously optimized for intraplaque hemorrhage detection [25], but variation in optimized thresholds for other MP-RAGE protocols is possible for other MP-RAGE parameters.

2.5.8 *Summary*

With histology validation, an optimized threshold of approximately 150% based on adjacent soft tissue has good intraplaque hemorrhage detection performance and thus is recommended where an adjacent soft tissue region of isointense with fibrous plaque can be readily identified and manually defined. For semi-automated intraplaque hemorrhage detection, an optimized threshold of approximately 200% based on local median value appears to be the optimal choice giving an accuracy similar to that of adjacent soft tissue. These optimized thresholds can be used not only for semi-automatic or automatic intraplaque hemorrhage detection in MP-RAGE images, but can also provide an objective criterion for manual detection of carotid intraplaque hemorrhage.

2.6 IN VIVO EXPERIMENT ON SNAP

2.6.1 *Imaging Population*

14 carotid atherosclerosis patients scheduled for carotid endarterectomy (CEA) were recruited from University of Washington Medical Center and Affiliated Hospitals and consented in the study. Study protocol was approved by the institutional review board. Written informed consent was obtained from enrolled subjects.

2.6.2 *MR Imaging*

All patients were scanned with 3T MRI (Philips R3.2.1, Best, The Netherlands) before surgery using an eight-channel carotid coil. The MR sequences included 3D SNAP (TR/TE/TI = 10/4.7/500 ms, acquisition resolution = 0.80×0.80×0.80 mm^3, reconstructed resolution =

0.40×0.40×0.40 mm^3) [32] and a conventional 2D multicontrast protocol (TOF, proton density weighted, T1-weighted and T2-weighted) [26]. The thickness of conventional MRI was 2mm.

2.6.3 *Data analysis*

Histology sections and reformatted axial SNAP images were matched indirectly by first matching each to the conventional 2D multi-contrast MR images. Matching between histology and multi-contrast images was based on lumen/wall morphology and the distance to carotid bifurcation to account for any distortion and variable shrinkage of the tissue [30]. Matching between SNAP and multi-contrast images was based on distance to the carotid bifurcation as both protocols were acquired sequentially in the same imaging session. As histological sampling was finer than the spacing between MR slices, multiple histological sections may be matched to a single MR image. In that case, intraplaque hemorrhage was defined as present on that slice if any of the matched histological sections showed intraplaque hemorrhage. Considering the limited resolution of SNAP compared to histology, slices with small intraplaque hemorrhage area ($\pi \cdot r^2 = 2.01$ mm^2, where r = 0.80 mm) defined in histology were excluded from analyses according to previous established criteria [30].

The max normalized signal intensity on SNAP on each image was compared to the presence/absence of intraplaque hemorrhage as defined on the matched histology sections to determine an optimal signal intensity threshold for detecting intraplaque hemorrhage, as described in Chapter 2.4 section above.

Additionally, the reformatted axial SNAP images were reviewed by two readers (eight and four years' experience in cardiovascular MR). intraplaque hemorrhage presence was determined in consensus by visually inspecting whether there were distinct hyperintense signals within the carotid wall. Agreement in intraplaque hemorrhage detection between histology and manual review, as well as automatic and manual review were evaluated using Cohen's kappa.

The sensitivity and specificity associated with the chosen threshold was estimated using leave-one-out cross-validation. One plaque was left out at each iteration rather than one slice, due to potential non-independence between slices of the same plaque. To retain the dependence between the images and histology slices from the same patient, images were resampled as clusters using R when calculating the confidence intervals. All statistical analysis was performed using R software (version 3.0.2).

2.6.4 *Results*

Patient information was summarized in Table 2-3. 116 MR slices with matched histology intraplaque hemorrhage information from 14 patients were generated. By excluding slices with small intraplaque hemorrhage bellow MRI detection resolution, 108 matched slices (36 with histology-detected intraplaque hemorrhage) were analyzed.

Table 2-3. Study Population

Characteristics	Number (N = 14)
Age (y)*	68.4 ± 9.7
Male	12 (86)
Symptomatic	3 (21)
Hypertension	11 (79)
Hyperlipidemia	14 (100)
Diabetes	3 (21)
Current smoker	5 (36)
Current statin user	14 (100)
Note: All numbers except age are numbers of patients, with percentages in parentheses. * Mean age ± standard deviation	

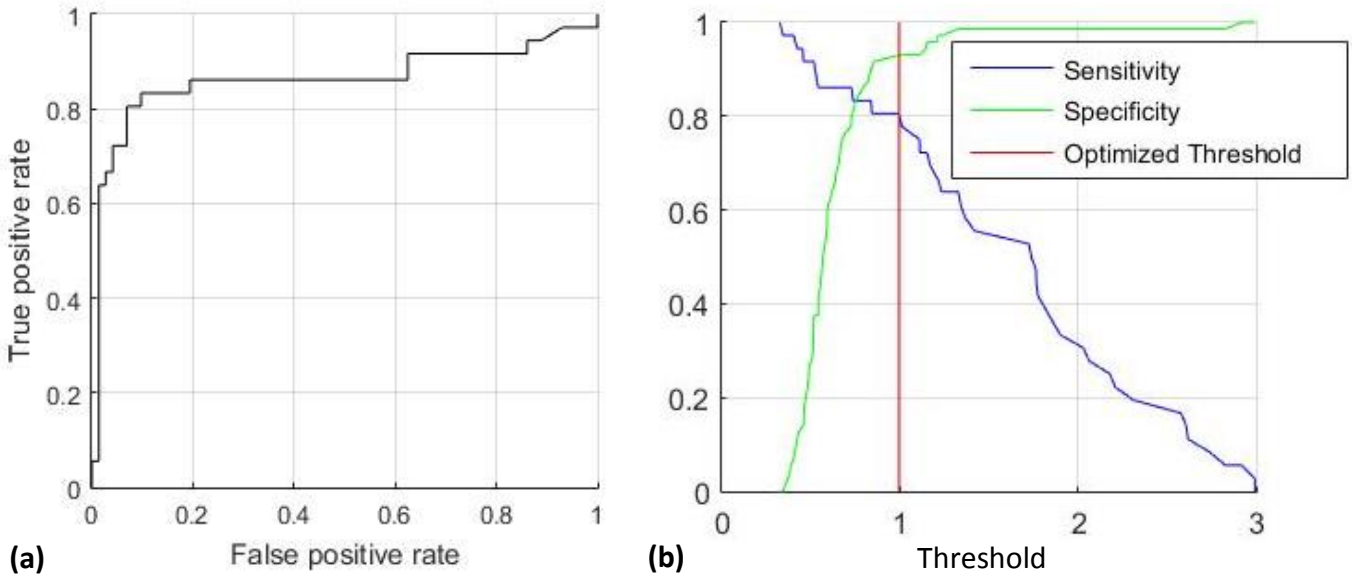

Figure 2-6. IPH detection performance in SNAP MRI using sternocleidomastoid muscle signal intensity on SNAP reference image for normalization. Receiver operator characteristic (ROC) curve (a) was used for intensity threshold optimization. Optimized threshold (red line in b) was chosen as the one that maximize Youden's Index (sensitivity + specificity – 1). Sensitivity and specificity curve with varying thresholds are also shown in (b) which can facilitate different threshold selection based on different goals.

The overall AUC for intraplaque hemorrhage detection was 0.83 (0.73, 0.93). The optimized hyperintensity threshold was identified as 1.0 of SCM signal intensity on I2 (Figure 2-6). The sensitivity and specificity were 76% and 88% based on cross-validation. If the 8 slices with small intraplaque hemorrhage were included, the optimized threshold was still 1.0 of SCM signal intensity on I2.

Manual review detected intraplaque hemorrhage in 35 MR slices from 8 plaques. The sensitivity and specificity were 83% and 93%, respectively. Both automatic (kappa: 0.72; 95% CI: 0.55, 0.85) and manual (kappa: 0.77; 95% CI: 0.59, 0.87) review had a moderate agreement with histology, whereas the agreement between automatic and manual intraplaque hemorrhage detection was high (kappa: 0.87; 95% CI: 0.75, 0.97).

2.6.5 *Discussions*

In this study, thresholds for intraplaque hemorrhage detection were optimized using intensity of SCM on SNAP reference image for intensity normalization and referring to histology as gold standard, resulting a semi-automatic method to identify intraplaque hemorrhage on SNAP.

The near-perfect agreement with manual review indicates that visual inspection of hyperintense areas is a viable approach despite being more time-consuming. This may be again attributable to high IPH-to-wall contrast in SNAP. Both manual and automated review showed a substantial agreement with histology. These findings highlighted some intrinsic limitations of MRI in characterizing intraplaque hemorrhage, including limited spatial resolution and possible

colocalization of intraplaque hemorrhage with calcification, as previously seen for other sequences [30, 34]. To ensure blinded analyses, matching between histological sections and reformatted SNAP images was performed indirectly by using 2D MR images as a bridge, which could also lower the agreement. Nonetheless, we expected that any mismatching should be random and not affect the signal intensity threshold.

The optimized thresholds were obtained by maximizing the sum of sensitivity and specificity, but Figure 2-6 can be used to choose a different threshold where higher sensitivity or specificity is required. For example, when screening patients for intraplaque hemorrhage a lower threshold value can be used to obtain a higher sensitivity for intraplaque hemorrhage.

Previous researches on MP-RAGE in detecting intraplaque hemorrhage manually have obtained sensitivity and specificity of 84% and 84% [24], 53-80% and 97% [30], respectively. In this study, sensitivity and specificity for intraplaque hemorrhage detection on SNAP MRI were 76% and 88%, respectively. It is not rigorous to compare intraplaque hemorrhage detection performance between SNAP and MP-RAGE with different study cohort. However, comparing with MP-RAGE, SNAP has the advantages such as 1) higher IPH-to-wall contrast, 2) less flow artifact [4] and 3) simultaneous lumen and intraplaque hemorrhage imaging.

The limitation of this study was that slice matching between SNAP and histology was not perfect. The reasons included 1) the histology specimen may be sectioned at a slightly different orientation compared with MRI slices; 2) the histology specimen may have different magnitudes of shrinkage during processing that varies depending on the presence and quantity of different

plaque components. However, the intraplaque hemorrhage detection performance was good despite the possible under-estimation due to mis-registration.

2.6.6 *Summary*

Using histological gold standard, this study developed a semi-automatic method to identify intraplaque hemorrhage on SNAP. The optimized threshold was 1.0 times SCM (mean sternocleidomastoid intensity) on SNAP reference image. Using the optimized intensity threshold, semi-automatically detected intraplaque hemorrhage had good intraplaque hemorrhage detection performance and high agreement with manual intraplaque hemorrhage detection.

Chapter 3. QUANTITATIVE MR CHARACTERIZATION OF CAROTID INTRAPLAQUE HEMORRHAGE

3.1 OVERVIEW

Although Chapter 2 established an objective approach for intraplaque hemorrhage detection, quantitative characterization of intraplaque hemorrhage on MRI may provide more information toward the vulnerability of intraplaque hemorrhage and its clinical risk, considering that intraplaque hemorrhage quantitative measures (volume [40] and intensity [38]) change more rapidly than intraplaque hemorrhage presence and that intraplaque hemorrhage quantitative measures differ between symptomatic and asymptomatic plaques [39, 41]. Therefore, semi-automatic and reproducible method for intraplaque hemorrhage quantitative measures is in great need for more insightful plaque vulnerability and progression assessment.

The goals of this study were two-fold. First, the study aimed to develop a time-efficient method for quantitative MR characterization (volume and intensity) of carotid intraplaque hemorrhage based on volumetric image processing and the optimized intensity threshold. Second, the study sought to evaluate the scan-rescan reproducibility of intraplaque hemorrhage signals, which were generated using the time-efficient volumetric image processing method.

3.2 Materials and Methods

3.2.1 *Imaging Population*

The study protocol was approved by the local institutional review board and written informed consent was obtained from all enrolled subjects. The study was compliant with the Health Insurance Portability and Accountability Act. Thirty-three patients with asymptomatic 16-99% carotid stenosis identified by ultrasound who did not meet clinical indications for CEA were recruited in this study. They underwent two SNAP scans within one month. Consecutive screening and enrollment of subjects occurred between June 2013 and February 2016, at the University of Washington Medical Center and Affiliated Hospitals.

3.2.2 *MR Imaging*

All scans were performed at 3.0-T (Philips, Best, The Netherland) with an 8-channel carotid coil [73]. SNAP is a recently developed inversion-recovery gradient echo sequence using phase-sensitive reconstruction [32]. The sequence design has been previously described in detail [32]. Two SNAP MRI scans were performed within one month. The SNAP protocol used for this study was consistent with the one used in Chapter 2, which was optimized for both IPH-to-wall contrast and flow-suppression [70]: repetition time/echo time = 10/4.8 msec, flip angle = 11°, inversion time = 500 msec, field-of-view = 160×160×32 mm^3, scan time = 5.3 minutes. Spatial resolution was 0.8×0.8×0.8 mm^3 acquired and interpolated to 0.4×0.4×0.4 mm^3 by the scanner.

3.2.3 *Quantitative Characterization of Intraplaque Hemorrhage Using Volumetric Image Processing*

SNAP image signal intensity was first normalized using the sternocleidomastoid muscle signal intensity on SNAP reference image (described in Chapter 2.3.3). A rapid intraplaque hemorrhage quantification method (Figure 3-1) with minimal human input was developed for evaluating the extent and magnitude of intraplaque hemorrhage signals in SNAP based on the signal intensity threshold of intraplaque hemorrhage as determined in Chapter 2.6. First, maximum and minimum intensity projections were automatically generated and overlaid to facilitate region selection. Second, a 3D box to delineate the ROI covering the carotid bifurcation was defined interactively on the compound display by selecting two points (left upper and right lower corners) in the coronal and sagittal views, respectively. The 3D ROI was wide enough to include any hyperintense areas if present, but avoided hyperintense areas that were distant from the carotid artery (e.g. peripheral regions with low coil sensitivity or poor fat saturation). Third, the mean SCM signal intensity on I2 was measured to normalize the signal intensity on SNAP, as described above. The optimized signal intensity threshold of intraplaque hemorrhage was applied to all voxels (0.4×0.4×0.4 mm3) in the 3D ROI box to obtain a binary 3D volume representing the presence/absence of intraplaque hemorrhage within each voxel. No vessel wall boundary was needed for intraplaque hemorrhage segmentation. Fourth, intraplaque hemorrhage regions were determined after a morphological opening with a 2×2×2 cubic as the structuring element which accounted for the lower acquired resolution (0.8×0.8×0.8 mm3). intraplaque hemorrhage volume was calculated as the number of voxels in all intraplaque hemorrhage regions multiplied by voxel size. Maximum normalized intensity of the 3D ROI and mean normalized intensity of intraplaque hemorrhage regions (if intraplaque hemorrhage was present) were recorded.

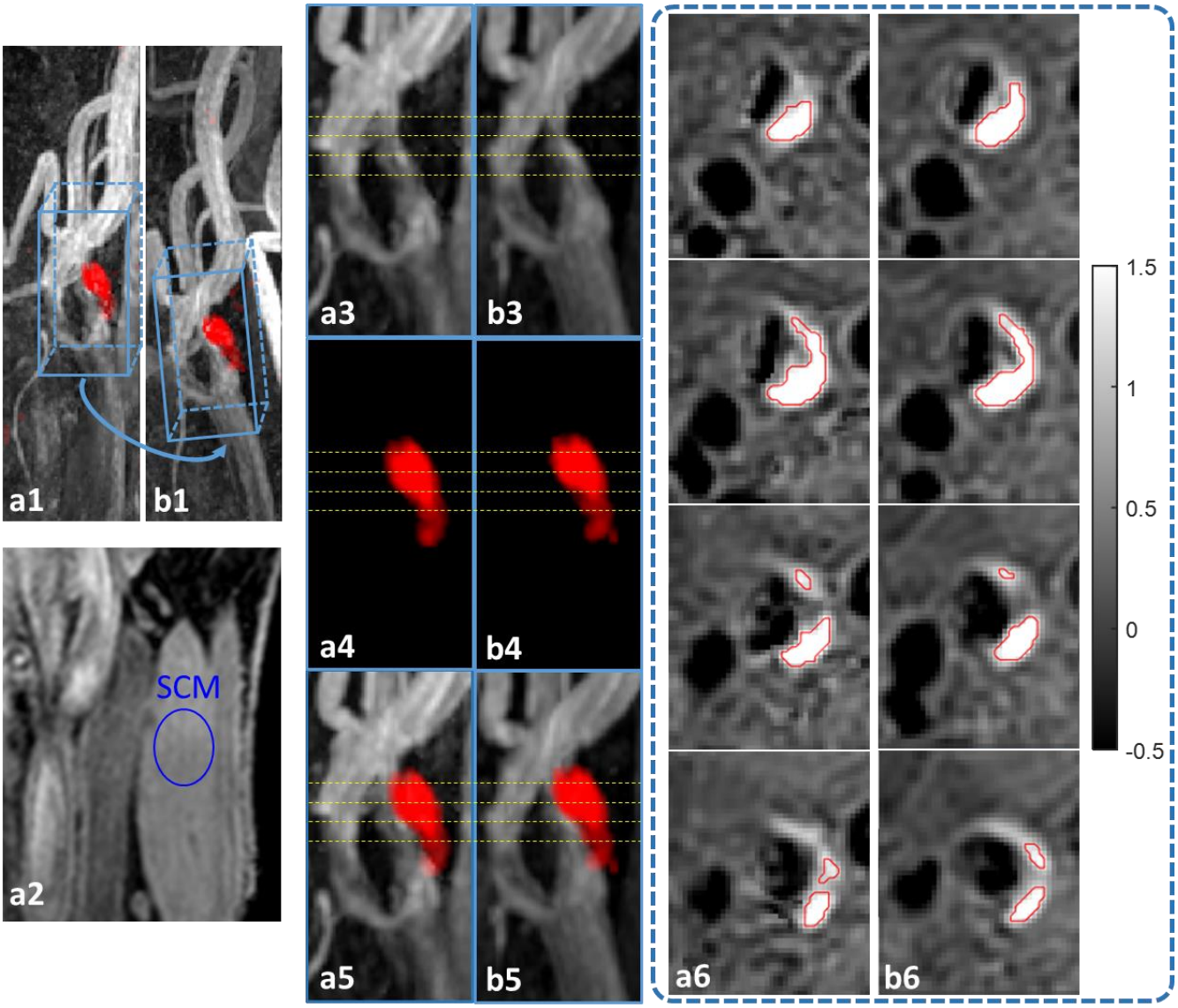

Figure 3-1. Using the rapid IPH quantification, IPH was segmented automatically in two repeated scans (a and b) with the optimized signal intensity threshold after 3D ROI was defined. At the first scan (a1), 3D ROI was defined interactively by selecting two points in coronal and sagittal views, respectively, and was mapped to the second scan (b1) with local rigid registration. 2D ROI for SCM was selected close to the common carotid artery bifurcation in coronal SNAP I2 image for each artery at each scan (a2). By zooming in the 3D ROI areas, MRA (white, mIP image, a3, b3), color-coded IPH (red, MIP image, a4, b4) and the combined view (a5, b5) show reproducible IPH imaging. Axial views (a6, b6) at the yellow dashed line levels show very similar segmented IPH boundaries between the two scans (red). The two scans occurred the same day. SCM = sternocleidomastoid.

3.2.4 *Reproducibility Studies*

In order to access the scan-rescan reproducibility, the 3D ROI defined on the first scan was automatically mapped to the second scan by local rigid registration (MATLAB, R2015a) with bicubic interpolation method. The mean SCM signal intensity on I2 was measured separately for each scan to normalize the signal intensity. After the 3D ROI was mapped to the second scan, the intraplaque hemorrhage measurements (intraplaque hemorrhage volume, maximum normalized intensity and mean normalized intensity of intraplaque hemorrhage) were calculated automatically and independently from each scan. This approach is also suitable for analyzing multiple follow-up scans in serial imaging studies.

3.2.5 *Statistical Analysis*

Cohen's kappa was used to assess scan-rescan reproducibility in presence of intraplaque hemorrhage signals. Intraclass correlation coefficient (ICC) and coefficient of variance (CV) were used for evaluating the reproducibility of maximum normalized intensity, intraplaque hemorrhage volume and mean normalized intensity of intraplaque hemorrhage. ICC of greater than 0.75 indicates strong agreement [74]; kappa values of greater than 0.81 and 0.61-0.80 were considered near-perfect and substantial, respectively [75]. The paired t-test was used to test differences between first and reproducibility scans.

To adjust for dependence between multiple measurements from the same subject (bilateral arteries), the non-parametric bootstrap and percentile method was used to calculate 95% confidence intervals (CIs) for kappa and ICC, which were expressed in parentheses. Spearman's

correlation coefficient was compared to 0 using a permutation test where the inter-scan time interval was permutated between subjects. Statistical significance was defined as $p<0.05$. All statistical analysis was performed using R software (version 3.0.2).

3.3 RESULTS

3.3.1 *Patient Characteristics*

33 subjects (68.4 years ± 9.7; 12 males) were recruited (Table 3-1). The mean inter-scan time interval was 7.8 days ± 8.9. Sixty-six carotid arteries were thus included in the reproducibility study.

Table 3-1 Study Populations

Characteristics	Number (N = 33)
Age (y)*	67.8 ± 14.7
Male	23 (70)
Symptomatic	0 (0)
Hypertension	27 (82)
Hyperlipidemia	31 (94)
Diabetes	6 (18)
Current smoker	6 (18)
Current statin user	26 (79)
Note: All numbers except age are numbers of patients, with percentages in parentheses. * Mean age ± standard deviation	

3.3.2 *Scan-rescan Reproducibility of Intraplaque Hemorrhage Signals on SNAP*

Maximum normalized intensity in SNAP showed high scan-rescan reproducibility with an ICC of 0.88 (95% CI: 0.74, 0.92) (Table 3-2). Using the histology-determined signal intensity threshold,

17 (26%) arteries were categorized as IPH-positive in both scans, 7 (11%) were categorized as IPH-positive in only one scan, and 42 (64%) were categorized as IPH-positive in neither scan, yielding a kappa of 0.75 (95% CI: 0.57, 0.91). The arteries showing intraplaque hemorrhage in only one scan were associated with a much smaller intraplaque hemorrhage volume compared to those showing intraplaque hemorrhage in both scans (3.0 mm^3 ± 5.0 versus 34.9 mm^3 ± 38.9; $p<0.001$).

Table 3-2**.** Scan-Rescan Reproducibility of Quantitative Measures from Volumetric Image Processing.

	All Arteries (N = 66)			IPH-positive in both scans (N = 17)				IPH-positive in at least one scan (N = 24)			
	ICC (95 % CI)	CV	Within-subject SD	ICC (95% CI)	CV	Within-subject SD	p*	ICC (95 % CI)	CV	Within-subject SD	p*
Maximum normalized intensity	0.88 (0.77, 0.93)	15.6 %	0.19	0.86 (0.57,0.96)	10.6 %	0.21	0.492	0.86 (0.70, 0.94)	12.8 %	0.22	0.102
IPH volume (mm^3)	-	-	-	0.99 (0.93, 1.00)	11.8 %	4.13	0.062	0.99 (0.94, 1.00)	16.2 %	4.06	0.022
Mean normalized intensity of IPH	-	-	-	0.77 (0.32,0.94)	5.2%	0.07	0.827	-	-	-	-

* Paired t-test between scan 1 and scan 2.
CI = confidence interval, CV = coefficient of variation, ICC = intraclass coefficient variation, IPH = intraplaque hemorrhage, SD = standard deviation.

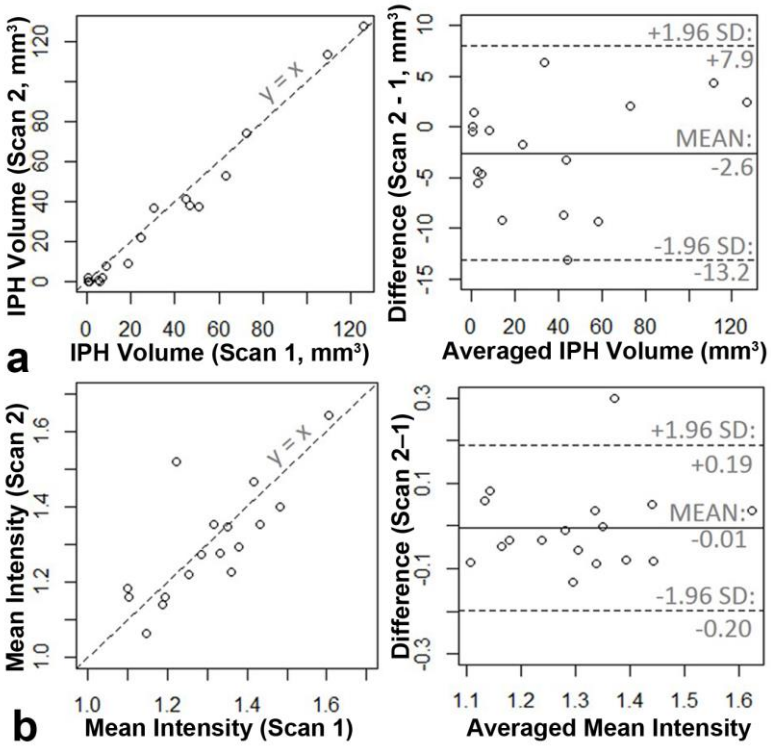

Figure 3-2. Scan-rescan reproducibility of quantitative measure of IPH signals. Scatter plots (left) and Bland-Altman plots (right) show the reproducibility of IPH volume (a) and mean normalized signal intensity (b) in the 17 arteries categorized as IPH-positive at both scans. Dashed lines in scatter plots are y = x lines.

Of the 17 arteries categorized as IPH-positive in both scans, quantitative measures of intraplaque hemorrhage signals showed high reproducibility and small measurement variability (Table 3-2). ICC favored intraplaque hemorrhage volume while CV favored mean normalized intensity of intraplaque hemorrhage. Bland-Altman plots indicated no apparent relationship between variance and mean for both measurements (Figure 3-2). There was no significant difference in mean normalized intensity of intraplaque hemorrhage between first and reproducibility scans. However, there was a trend towards a lower intraplaque hemorrhage volume in the reproducibility scan (36.2 mm^3 $\pm$ 38.3 versus 33.6 mm^3 $\pm$ 39.7; p=0.062). When analysis of intraplaque hemorrhage signals was extended to the 24 arteries categorized as IPH-positive in at

least one scan, a significant decrease in intraplaque hemorrhage volume was seen in the reproducibility scan, accompanied by a trend of decrease in maximum normalized intensity (Table 3-2). The inverse registration (scan 1 registered to scan 2) also confirmed similar results.

3.4 DISCUSSION

To our knowledge, this is the first study to describe a volumetric image processing method for quantitative characterization of carotid intraplaque hemorrhage. It leverages the unique dual contrast of SNAP MRI to achieve time-efficient intraplaque hemorrhage quantification and can be easily applied to other vascular beds where artery tortuosity poses a bigger challenge and histological data are more difficult to acquire [76, 77]. Using this method validated with histology and manual review, our study also provides a detailed evaluation of scan-rescan reproducibility of intraplaque hemorrhage signals on MRI. It was noted that intraplaque hemorrhage signals may evolve more rapidly than currently understood, although short-term changes appeared subtle and may be only detectable with automatic analysis. Methods and findings from this study can be easily adopted in future serial studies to expand our knowledge on the risk factors and effective therapies of intraplaque hemorrhage.

Most previous studies focused on the presence or absence of high T1 signals when studying high-risk plaques. However, recent studies suggested that quantitative measures of T1signals may serve as novel biomarkers for understanding the substantial heterogeneity among intraplaque hemorrhage plaques and monitoring intraplaque hemorrhage progression [38-41, 78]. In a study of 31 patients with recent cerebrovascular ischemic events and bilateral carotid intraplaque

hemorrhage, Wang et al [41] found that intraplaque hemorrhage plaques on the symptomatic side had stronger and more extensively distributed T1 signals than those on the asymptomatic side. Both intraplaque hemorrhage progression and regression have been observed by measuring the extent or strength of T1 signals in 1-2 years [38-40]. Whether these changes reflect underlying tissue repair or repeated intraplaque hemorrhage remain unclear. In a serial study of coronary plaques, Noguchi et al [78] found that 12-month pitavastatin treatment resulted in a significant decrease in normalized T1 signal intensity compared to a significant increase in the control group. The quantitative, reproducible approach to the assessment of high T1 signals as developed and validated in this study will greatly facilitates future research on this topic.

Few studies have reported scan-rescan reproducibility of intraplaque hemorrhage signals on MRI. A few practical, technical, and biological reasons are likely accountable (see *Introduction*). The lack of time-efficient methods to perform quantitative, reproducible review is a major technical barrier. Using multicontrast MRI, Touze et al [79] reported ICCs of 0.70 (95% CI: 0.52, 0.85) and 0.60 (95% CI: 0.37, 0.81) for intraobserver and interobserver reproducibility, respectively. Inversion-recovery prepared gradient echo affords higher IPH-to-wall contrast [30], which may improve reproducibility of intraplaque hemorrhage signal measurements. By using phase-sensitive acquisition to increase the dynamic range of image contrast, SNAP further increases IPH-to-wall contrast and avoids flow artifacts, which may further improve reproducibility of intraplaque hemorrhage signal measurements. The strong negative signal of flowing blood can be exploited to facilitate time-efficient volumetric image processing, as shown in this study.

To our knowledge, only one previous study evaluated scan-rescan reproducibility of intraplaque hemorrhage signals on MRI [80]. A Pearson's correlation coefficient of 0.97 was reported for intraplaque hemorrhage volume in 12 carotid arteries scanned twice within two weeks using a semi-automated segmentation algorithm. Compared to the previous study, the method described here does not require manual seed points of intraplaque hemorrhage for initialization. It works on 3D data directly and may thus handle tortuous arteries. Furthermore, our method was developed and validated against histology rather than manual review, which avoided the measurement error introduced by subjective manual review.

With quantitative, reproducible measures of intraplaque hemorrhage signals afforded by the proposed method, this study found the first evidence of rapid yet subtle changes in intraplaque hemorrhage signals in a short study period. It indicates that methemoglobin from erythrocyte degradation was being cleared, at least partly, from atherosclerotic plaques. Intraplaque hemorrhage volume appeared to have higher reproducibility than mean signal intensity of intraplaque hemorrhage, which could explain why differences between first and reproducibility scans were primarily seen in intraplaque hemorrhage volume. An unsolved question is whether histogram analysis of intraplaque hemorrhage signal intensity at the voxel level may provide additional information. It is possible that repeated intraplaque hemorrhage may develop locally, leading to a local increase in signal intensity, while overall intraplaque hemorrhage volume and mean signal intensity may decrease.

Compared to previous reproducibility studies [44-46], we adopted imaging inclusion criteria to enrich our study sample with carotid plaques. However, this study remains limited by the small

number of intraplaque hemorrhage plaques. Particularly, the finding of rapid intraplaque hemorrhage signal evolution needs to be further studied using a larger study population. This finding also suggest that the reproducibility metrics as reported here may represent a conservative estimation of the true reproducibility of these quantitative biomarkers.

3.5 SUMMARY

We described a time-efficient method based on volumetric processing of dual contrast SNAP data for quantitative characterization of carotid intraplaque hemorrhage with minimal human input. The method was found to provide reproducible measures of intraplaque hemorrhage volume and signal intensity, which may serve as novel biomarkers and facilitate serial studies.

Chapter 4. MOTION DETECTION AND CORRECTION FOR CAROTID MRI USING STRUCTURED LIGHT

4.1 OVERVIEW

In establishing intraplaque hemorrhage (IPH) analysis methods, one common challenge arose from degraded image quality due to patient motion. Blur and ghost motion artifacts highly impact carotid MR image quality, reducing the accuracy of intraplaque hemorrhage delineation and quantitative measures of both intraplaque hemorrhage and reference signals. Indeed, patient motion has been a major challenge for MRI, and clinically applicable and robust motion correction technique could greatly enhance diagnostic yield.

The research goal of this specific aim was to develop a non-marker-attached motion detection and correction system targeted at carotid MRI, which is capable of detecting and correcting carotid abrupt motion (like cough and swallowing) and bulk motion, with the merits of sequence independence and no patient interaction.

In order to accomplish this goal, the following studies were conducted: 1) motion detection system based on structured light [81] was built inside the MRI scanner bore to record the motion of the object; 2) for abrupt motion, such as cough and swallowing, motion correction based on parallel imaging was developed; 3) for bulk shift motion, phase correction was implemented with rigid motion assumption.

4.2 MOTION DETECTION

4.2.1 *Theory*

Structured light (parallel lines, grid or other patterns) has been used for depth measurement with high accuracy and is non-contact with the object [61, 81]. When the light hits the surface of the object, different depth will be reflect as different light position in the camera image plane. In Chen et al.'s research on surface height measurement based on structured light, the sensitivity was 0.18 mm/ pixel and the accuracy was around 0.06 mm with their system layout [61]. Therefore, structured light can accurately detect depth information without any attached markers.

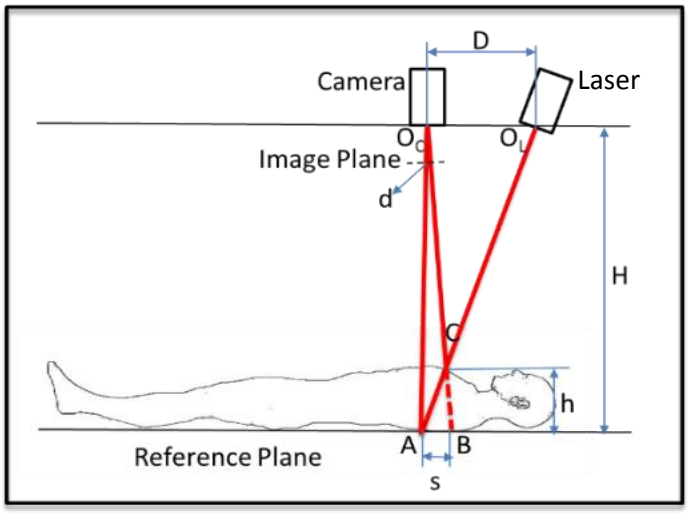

Figure 4-1. Optical motion detection system. Camera can capture the projected laser shift caused by the height (h) change of the patient.

The theory of optical motion detection method was based on triangle measurement, as shown in Figure 4-1. The height of the subject (h) could be calculated based on the laser position (d) in the image plane of the camera (Figure 4-1), using a similar triangle calculation,

$$h = \frac{dkH}{D + dk}$$

, where k is the length ratio of the object and its image, H is the distance between the camera and the reference plane, and D is the distance between the camera and the laser projector.

4.2.2 *Hardware Setup*

The optical motion detection system was set up inside the bore of a 3T whole body MR scanner (Philips, Best, The Netherlands). A laser (GM-CR02, Apinex, Canada) projected a green cross line on the subject, which was captured by a MR-compatible camera (12M, MRC, Germany) with a frame rate of 30 frames per second. A video cable transmitted the video to a laptop workstation (Windows 7, i7-4810MQ CPU @ 2.80GHz, 8.00 GB RAM, DELL, USA) after passing a penetration panel and a filter box (MRC, Germany).

4.2.3 *Image Acquisition and Processing*

Video data was collected and processed using LabVIEW (v2013, USA) during MR scans (Figure 4-2). The coordinate of the center of cross line in each video frame was calculated by real-time pattern matching algorithm and was recorded every 2 ms. Low-discrepancy sampling method was used in pattern matching algorithm and subpixel accuracy was enabled.

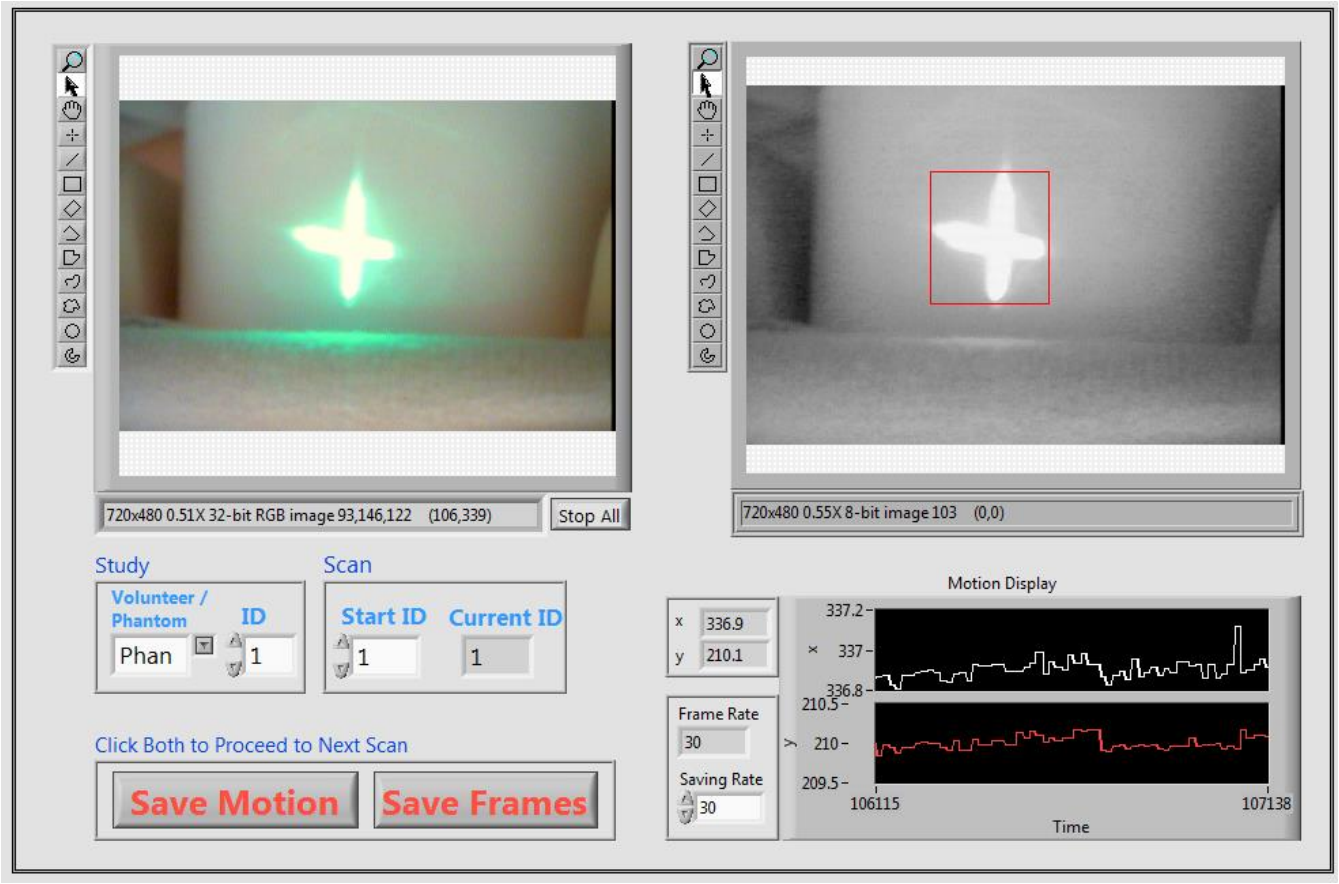

Figure 4-2. LabVIEW panel for motion detection. Green laser cross was projected onto a bottle phantom during the MR scan. The video data was acquired as RGB images and transferred to gray images using their intensity value. By comparing with a laser cross image template generated for each object, the location of laser cross on each frame was determined using pattern matching and recorded for each MR scan.

4.2.4 *System Calibration*

In order to get the relationship between object height, h, and laser position, d, calibration was performed by recording the laser position of subjects of known heights. The heights of subjects used for calibration were 72, 84, 96, 108, 120 mm. The relationship between h and d were fitted utilizing nonlinear least square curve fitting (MATLAB, R2010b, USA).

4.2.5 *Abrupt and Bulk Motion Detection*

Edge detection based on Canny's method [82] was used to detect abrupt motion, which has a relatively quick change. It was combined with monotonicity detection to accurately locate the time when abrupt motion started or ended. Edge detection was choose over amplitude thresholding to avoid bulk motion effect. After the time of motion was identified and adjusted by subtracting the time delay, the corresponding corrupted k-space lines were located.

For bulk shift motion, which could easily happen around the abrupt motion, median value of the laser location in the camera image before and after the abrupt motion period were calculated. The location differences ($\Delta d = d_1 - d_2$) were recorded.

4.3 MOTION CORRECTION

In order to find the corresponding k-space lines with the motion occurring time information, the time of each k-space line acquisition was recorded in a log file during MR scans by editing and generating patch file using Philips Paradise software.

With the motion information measured by the structured-light system during MR scans, the MRI raw data (k-space data) were exported after the scan and reconstructed retrospectively in the following steps.

4.3.1 *Abrupt Motion Correction*

The abrupt motion in the neck area is non-rigid and thus is hard to correct by just phase adjustment. Since abrupt motion duration is short, the corresponding corrupted k-space lines could be deleted and re-estimated using parallel imaging reconstruction methods. In this study, Iterative Self-consistent Parallel Imaging Reconstruction (SPIRiT) was selected over generalized autocalibrating partially parallel acquisitions (GRAPPA) [83, 84] since it showed better image reconstruction quality in our experiments.

4.3.2 *Bulk Shift Motion Correction Using Initial Distance Estimation*

Bulk motion caused by shifting position or rotating head is unavoidable during MR scans, especially after abrupt motion. This kind of bulk motion could last for a long duration and thus it is not feasible to be corrected by deleting all the corresponding k-space lines. Since the bulk motion happens in the narrow space within the scanner bore and attached carotid coil, it was assumed as rigid motion and thus phase correction was performed to adjust the location difference before and after abrupt motion based on the initial distance estimation according to system calibration.

Using structured light motion detection system (Figure 4-1), the anterior-posterior translation ($\Delta h = h_1 - h_2$) can be calculated based on the recorded shift of the laser ($\Delta d = d_1 - d_2$) from the captured images. As discussed in Chapter 4.2.1,

$$h = \frac{dkH}{D + dk}$$

Therefore,

$$\Delta h = h_1 - h_2 = \frac{[d_1 kH(D + d_2 k) - d_2 kH(D + d_1 k)]}{(D + d_1 k)(D + d_2 k)} = \frac{(d_1 - d_2)kHD}{(D + d_1 k)(D + d_2 k)}$$

$$= \frac{\Delta d kHD}{(D + d_1 k)(D + d_2 k)}$$

If $D \gg d_1 k, d_2 k$, then $D + d_1 k \approx D + d_2 k$, we can further simplify the equation to

$$\Delta h \approx \frac{\Delta d kHD}{(D + d_1 k)^2}$$

When $D \gg d_1 k, d_2 k$, the relationship between Δd and Δh can be simplified as a linear relationship, which can be obtained by system calibration.

The phase correction for bulk shift was based on Fourier Transform property that translation in image space corresponding to added phase in frequency space:

$$\mathbb{F}\{f(x - x_0, y - y_0)\} = F(u, v)e^{-i2\pi(\frac{ux_0 + vy_0}{N})}$$

, where $\mathbb{F}$ means Fourier Transform, and $F(u, v) = \mathbb{F}\{f(x, y)\}$.

4.3.3 *Bulk Motion Correction Using Optimized Distance Estimation*

In this study, only two dimensional in-plane motion was considered in this 2D MR scan. Only one dimension of motion in the anterior-posterior direction was recorded but the bulk motion could also happen in the left-right direction. Therefore, every point in the vicinity of the initial distance estimation was used as translation parameter to calculate the 2nd order sharpness of reconstructed image. Neck shift was corrected using optimized translation parameters with maximized sharpness of reconstructed image (Figure 4-3).

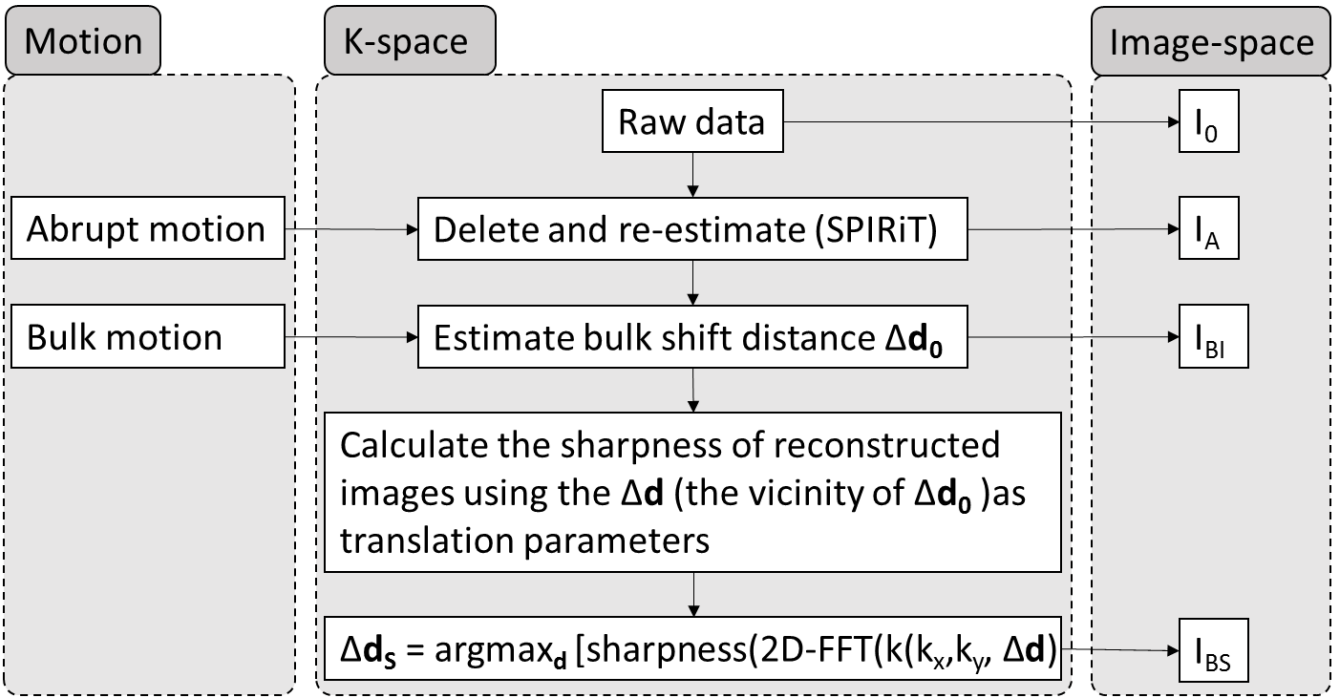

Figure 4-3. Motion correction steps for both abrupt motion and bulk motion. Images without motion correction (I_0), with only abrupt motion correction (I_A), with both abrupt motion and bulk motion correction (initial estimation) (I_{BI}) and with both abrupt motion and bulk motion correction (sharpness optimized) (I_{BS}) were reconstructed.

4.4 Phantom Motion Correction Experiments

4.4.1 *Image Acquisition*

A phantom bottle was scanned on 3T MR scanner (Philips, Achieva, The Netherlands) with 8-channel neck coil. 2D Fast Field Echo (FFE) MRI protocol was used with the following parameters: TR/ TE = 100 / 5.2 ms, flip angle = 20°, FOV = 200×200 mm^2, resolution = 1.0 mm, slice thickness = 5 mm.

During the MR scan, abrupt motion was introduced by manually lifting the phantom in vertical direction for a short duration (around 1s) and returning to its original position. Bulk shift motion

was introduced by shifting the phantom position. Abrupt motion and bulk shift motion were introduced to different MR scans and were corrected separately retrospectively.

4.4.2 *Time Synchronization*

In order to accurately find the corresponding corrupted k-space lines when motion occurs, time between the laptop which was used to record motion and the MR scanner should be synchronized accurately. The accuracy should be within several milliseconds, considering that the repetition time (TR) for one k-space line could be as small as a few milliseconds. Therefore, the time was synchronized using Network Time Protocol (NTP), which has time accuracy better than 1ms within local network [85].

However, there was still time difference between motion occurred and recorded due to the delay caused by image acquisition and processing. Therefore, an experimental method using LabVIEW (version 2013, USA) was developed to record the time delay caused by image acquisition and processing. The current changing time of the laptop (T1) was displayed in the panel (
Figure 4-4) as both numbers and graphics (showing increasing second and millisecond as rectangles as increasing heights) in the panel on the screen. The displayed rectangle was captured by the camera and its height was calculated and transferred back to millisecond, using similar pattern matching methods as in motion detection. Therefore by comparing the calculated time after image acquisition and processing and the current time of the laptop, the time delay was recorded. The same procedure was repeated for 15 times.

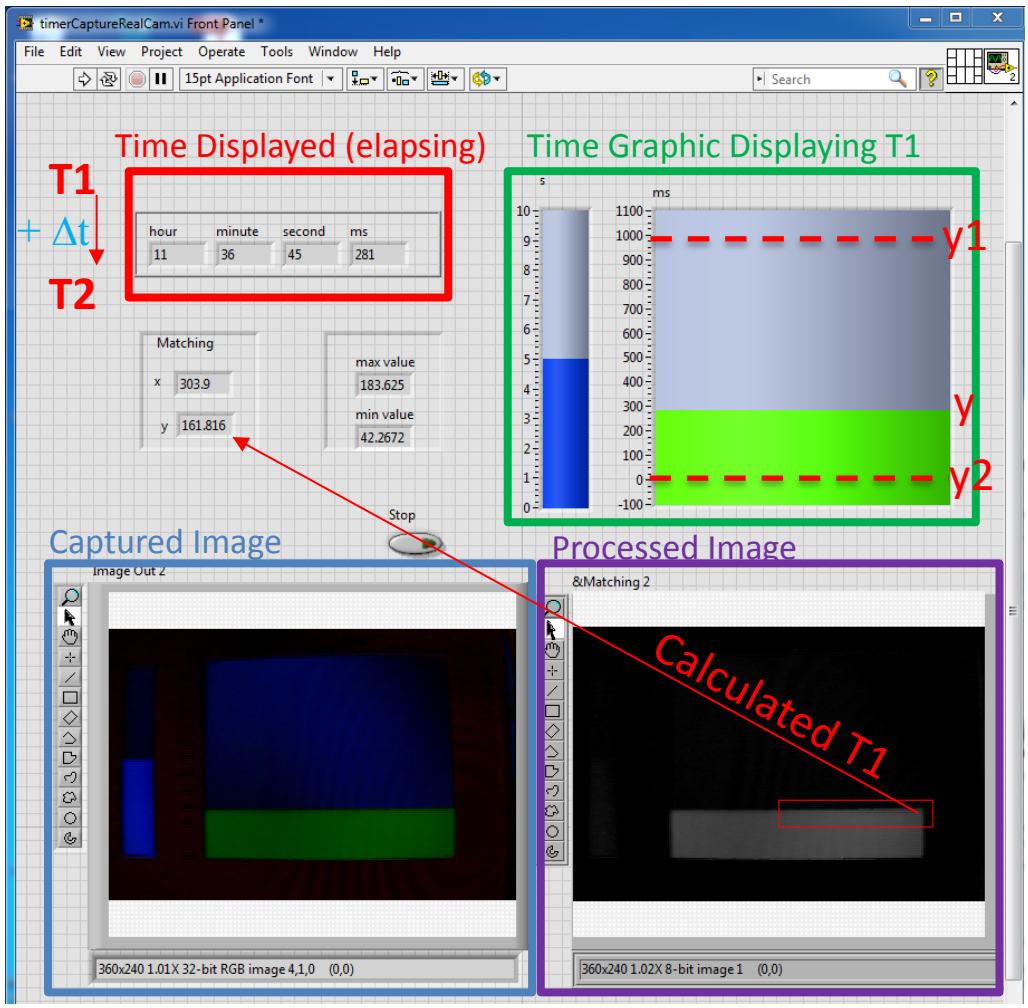

Figure 4-4. LabVIEW panel for time delay experiments. Current time (T1) was displayed as numbers and rectangles (increasing height corresponding to increasing second and millisecond). After being captured by the camera, the height of right rectangle was calculated and transferred to corresponding millisecond (T1). By comparing the current time of the laptop (increased to T2) and calculated time (T1), the time delay (Δt) was recorded.

4.4.3 *Results*

The system calibration result was shown in Figure 4-5. With the increasing pixel position, relationship between h and d was increasingly closer to a linear relationship. With this obtained calibration line, unknown heights of object can be calculated accurately given each pixel position d.

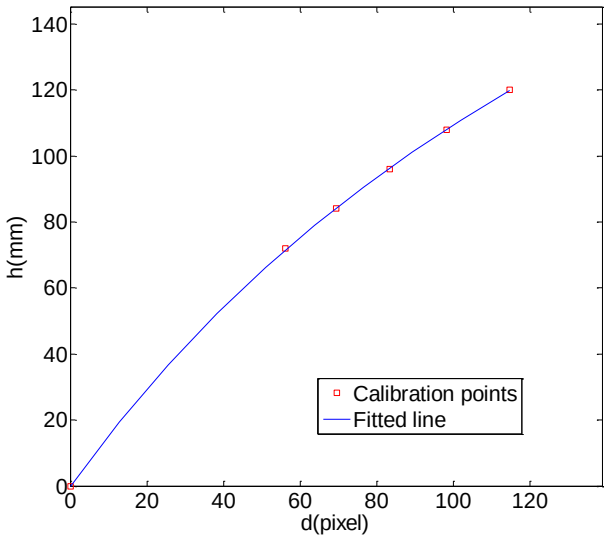

Figure 4-5. Relationship between height of subject (h) and pixel shift (d), obtained by calibration using subjects with known heights (h). Line was fitted using nonlinear least square curve fitting.

The time delay caused by image acquisition and processing was 109.6 ± 23.1 ms (mean ± standard deviation) based on the 15 experimental measurements.

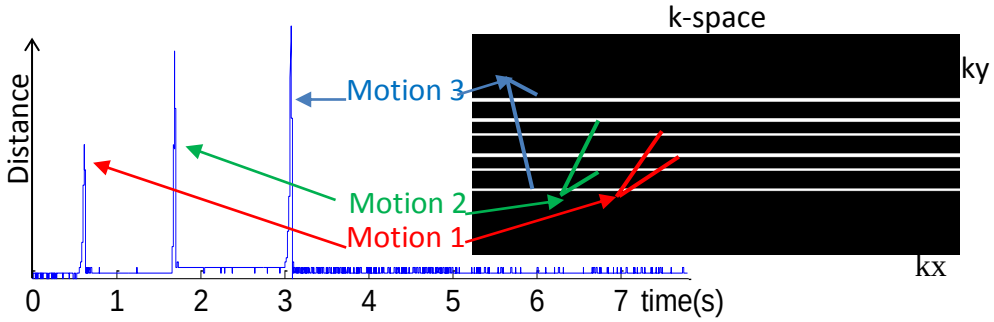

Figure 4-6. Laser location across time during phantom scanning.Three abrupt motions were detected (left). The corresponding corrupted k-space lines were localized (white lines, right), deleted and re-estimated using SPIRiT algorithm.

For motion detection, manually introduced motion on the phantom can be readily detected by tracking the shifting of laser. The recorded motion was matched to corresponding corrupted k-space lines. One phantom motion detection example was shown in Figure 4-6 with three manually

introduced motion readily identified. The corresponding corrupted k-space lines were located by checking the time stamps.

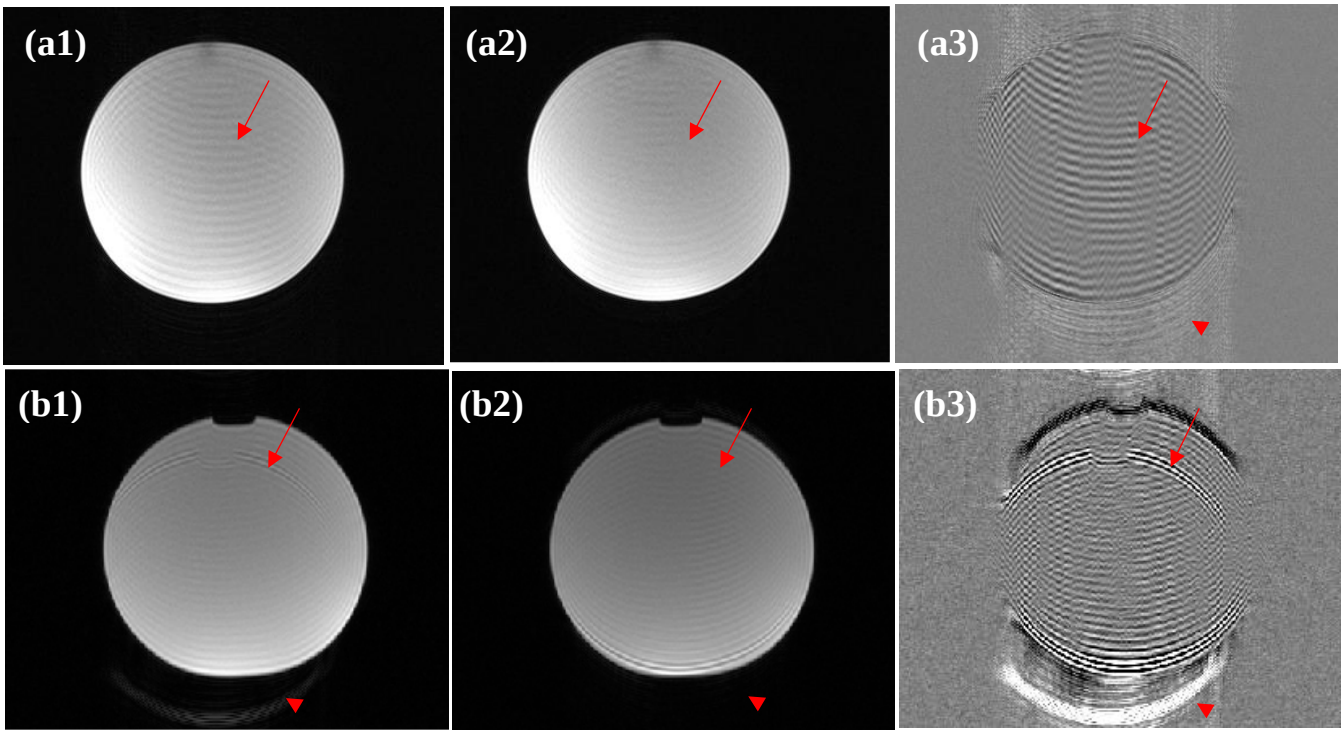

Figure 4-7. Phantom MR Images before and after motion correction. Abrupt motion (a) and bulk shift motion (b) were introduced respectively. In the original images (b1) shifted boundary induced by bulk shift was observed. After motion correction by added phase, image quality was improved with less motion artifacts (b2). The difference (x5) between original image and motion corrected image were shown in a3, b3. Red arrows point to the reduced motion artifacts inside the object while red arrow heads point to the reduced motion artifacts outside the object.

The abrupt motion introduced inhomogeneity to the image (Figure 4-7, a1). After re-estimating corrupted k-space lines, most of the motion artifacts were removed, including artifacts both outside and inside of the object (Figure 4-7, a2). And after motion correction, the phantom image was more homogenous with less strip artifacts.

The bulk shift motion during image acquisition was detected by the structured light system, which produced motion artifact of shifted boundary in the original MR images (Figure 4-7, b1). After phase correction for the bulk motion, the motion artifacts were effectively reduced (Figure 4-7, b2).

4.4.4 *Discussion*

Using phantom MR scans and manually introduced motion, the feasibility of detecting and correcting both abrupt motion and bulk motion for 2D MR scans was demonstrated.

One limitation of the current motion detection system is the relatively long delay of image acquisition and processing. However, the pattern matching algorithm only took around 10 ms and most the the delay should come from the camera image acquisition. Reducing standard deviation of time delay could also locate the corresponding corrupted k-space lines more accurately, especially when TR is small. If motion correction is performed retrospectively, image processing for laser position calculation could be done off-line, to further reduce the standard deviation of time delay. However, since the current frame rate was 30 frames per second (fps), the time interval between frames was around 33ms, limiting the accuracy of time delay. Therefore, in this study, TR was selected as bigger than 33ms to locate corrupted k-space lines. If TR smaller than 33ms has to be used, the neighbor of the calculated k-spaces lines should also be considered corrupted. In addition, the time delay accuracy was expected to be further reduced if a camera with higher frame rate was used. The current high speed camera in the market could be more than 10, 000 fps, resulting only 0.1ms duration for each frame. Therefore, accurately locate corrupted

k-space lines with much smaller TR is possible with higher speed camera and off-line image processing.

4.5 Volunteer Carotid MRI Motion Correction Experiments

Carotid artery wall imaging requires high-resolution black-blood MRI, but its image quality is often degraded by neck motion. The neck area has very complex motion pattern due to superposition of abrupt motion like swallowing and cough and bulk neck shift. In the previous section, it has been demonstrated that it is feasible to correct both abrupt and bulk shift in phantom MRI using structured light. This study aimed to separate different motion components and correct them for 2D carotid artery wall imaging, using non-marker-attached structured light system.

4.5.1 *Image Acquisition*

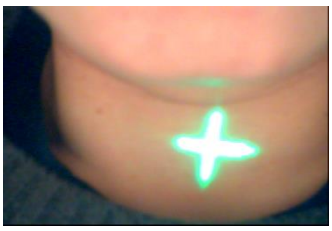

Figure 4-8. A green cross laser was projected on the neck of subjects to monitor the motion during MR scans.

A healthy volunteer was scanned for 2D black-blood carotid artery wall imaging using 8-channel carotid coil and 3T MR scanner (Philips, the Netherlands). 2D FFE sequence with saturation band was used: TR/TE = 100/5.4 ms, flip angle = 20° , FOV = 200 × 200 mm^2, resolution = 1.0 × 1.0 mm^2, slice thickness = 5 mm. For the first scan, the subject was instructed to avoid voluntary

motion, while for the next ten scans, the subject was instructed to swallow during five scans and to raise head shortly during the other five scans. K-space trajectory was low-high (e.g. 0, -1, 1, -2, 2 …) to make the k-space lines acquired during a short time more sparse. Laser was projected onto the neck area and monitored by the camera during MR scans.

4.5.2 *Motion Detection and Correction*

Respiration motion were extracted by applying low pass filter (cutoff frequency = 0.6 Hz). Abrupt motion was determined by edge detection. By referring to the optical system calibration, the initial distance estimation of bulk neck shift before and after abrupt motion was calculated. For the ten scans with voluntary motion, the raw data was reconstructed using MATLAB (R2015a, USA) with the following three steps for motion correction: (1) k-spaced lines acquired during abrupt motion was deleted and re-estimated using SPIRiT algorithm [83]; (2) the initial bulk shift distance was estimated and every point in its vicinity was used as translation parameter to calculate reconstructed image sharpness; (3) bulk neck shift was corrected using optimized translation parameters with maximized sharpness of reconstructed image.

4.5.3 *Results*

The respiration (16.9 ± 1.0 Rate/min), abrupt motion and bulk neck shift can all be separated from the optical motion detector (Figure 4-9). Averaged amplitudes for abrupt/ bulk/ respiration motions = 0.99/0.21/0.17 mm. For all the ten scans with voluntary abrupt motion, unconscious bulk neck shift were also detected after abrupt motion.

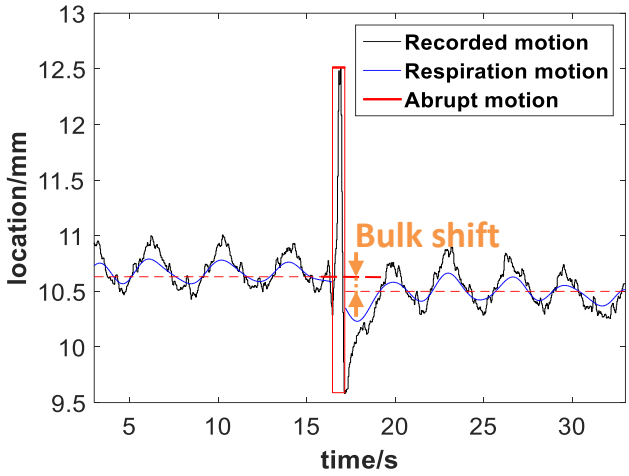

Figure 4-9. Original recorded motion and separated respiration, abrupt motion, bulk neck shift.

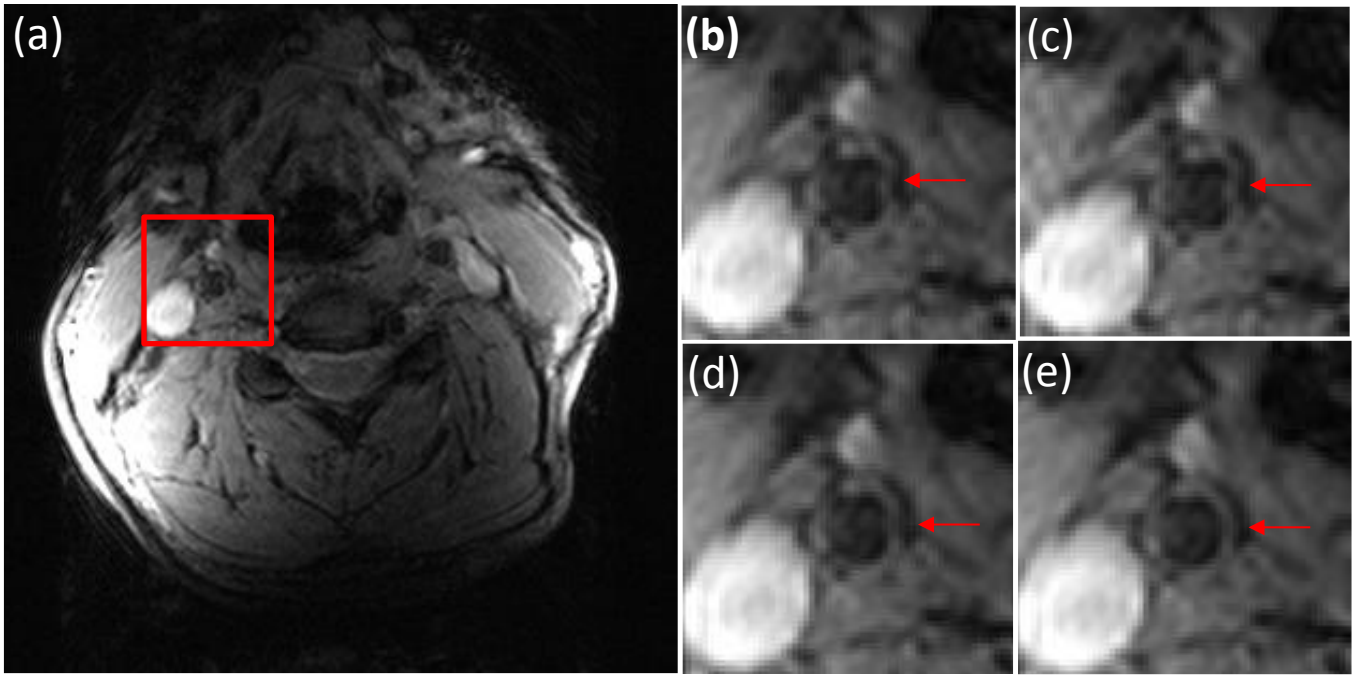

Figure 4-10. Motion correction for carotid artery wall using structured light. (a) is the original motion corrupted image with full FOV and (b-e) are zoomed in images: (b) original image (c) reconstructed image with only abrupt motion correction, (d) reconstructed image with both abrupt motion and bulk shift correction (with the initial distance estimation), (e) reconstructed image with both abrupt motion and bulk shift correction (with sharpness maximized). Arrows point to right carotid artery.

The scan without voluntary motion (but with respiration motion) and four scans with abrupt motion affecting less than 7.0% peripheral k-space lines still had delineable contours of vessel wall. The other six scans had severe motion artifacts, which were successfully removed except for two scans with multiple swallowing affecting a large range of k-space lines (17.7% and 31.6%, respectively). One motion correction example was shown in Figure 4-10. With abrupt motion and bulk neck shift correction (shift distance optimized by maximizing sharpness), the motion artifact in vessel wall area was removed, enabling more accurate vessel wall contour delineation.

4.5.4 *Discussion*

Carotid artery wall imaging has challenging motion issues due to the complex neck motion pattern. This study demonstrated that non-marker-attached structured light system can effectively detect abrupt motion, bulk shift motion and respiration in the neck area. Respiration motion was not corrected since it introduced much less motion artifact than abrupt motion or bulk neck shift in carotid artery wall imaging. It was also shown that unconscious bulk neck shift often follows abrupt motion, both of which can be corrected by structured light system.

The total duration of abrupt motion can affect not only the amount of motion artifact, but also the effectiveness of motion correction. Also, maximizing reconstructed image sharpness to optimize bulk shift distance can further improve the vessel wall delineation.

It was noticed that when bulk motion happened, there tend to be more motion artifacts affecting the carotid artery wall delineation than cases with only abrupt motion such as cough and swallow. The reason is probably that bulk motion could affect larger portion of k-space data than abrupt

motion. Also, bulk motion is often inevitable after cough or swallowing, since it is hard for the neck to precisely return to the same place before cough. Therefore, bulk motion correction is as important as, if not more important than, abrupt motion correction for carotid MR images.

Previous research showed that patients with more serious sickness tend to have more serious motion-related MR image quality issues [48]. For atherosclerosis patients, most of them are old patients who already suffered from plaques and may also have other health issues. Compared with other healthier people, it is harder for them to stay still without swallowing, cough or bulk motion, making motion a serious problem for carotid plaque imaging. Meanwhile, it is critical to clearly capture the plaque components, such as intraplaque hemorrhage, in order to access the vulnerability of plaques [4]. Furthermore, this proposed motion detection and correction system is non-attached to the patient and independent of the MR sequence, with both abrupt motion and bulk motion correction ability, and thus is promising in both clinical and research carotid MR scans.

One limitation of the current work was that only the coordinate of laser center was recorded and therefore sharpness optimization was needed for bulk shift distance optimization. However, the location of the whole laser line can be recorded to get more motion information. In addition, the phase correction could only compensate for rigid shift motion. But bulk motion in the neck area is often complex non-rigid motion, introduced by head movement or body shift. When bulk motion has a big amplitude and may not be assumed as rigid, more sophisticated algorithm for non-rigid motion compensation would be needed.

4.5.5 *Summary*

In summary, structured light motion detection system is able to detect both abrupt motion and bulk motion. Abrupt motion with short duration could be corrected by parallel image reconstruction methods. Maximizing reconstructed image sharpness to optimize bulk shift distance can further improve the vessel wall delineation.

4.6 RESPIRATION MOTION TRACKING AND VALIDATION

Respiration belt and navigator gated MR techniques have been widely used to detect respiration motion. While navigator techniques are widely available, they increase scan times, are not compatible with all sequence types, or are only usable if the thorax/abdomen are within the field-of-view. The respiratory belt is an alternative that can work in the above situations, but it is difficult to position and may have drifting problems [59].

In the previous section, it was demonstrated that respiration was detectable using this optical system. Therefore, we sought to detect respiration motion accurately and robustly using a structured light system which is MRI-independent and non-attached to the subject.

4.6.1 *Respiration Motion Detection*

Six healthy volunteers (5 female and 1 male) were recruited for this study. The study protocol was approved by institutional review board. Written consent form was obtained from each volunteer.

A laser and a MR-compatible camera (MRC, Germany, frame rate = 30 fps) were mounted above the subject on the patient bed inside the scanner bore (Philips Ingenia 3T, Best, the Netherland). A cross laser light was projected onto the neck area of the subject, which was captured by the camera. Based on structured light theory, the height of the object can be calculated based on the pixel location in the camera image with calibration using a set of objects with known heights. During the MRI scans, the y-coordinate of the cross center was calculated and recorded in real time for each frame using pattern matching (LabVIEW, v2013).

4.6.2 *Respiration Motion Validation*

A bandpass filter (Butterworth, cutoff frequency of 0.1 Hz and 0.5 Hz) was applied to the original motion record (MATLAB, 2014b) to remove bulk motion and other high frequency noise like pulsation. During the MRI scans, respiratory belt (Philips, Best, The Netherland) was also used to simultaneously record the respiration motion. The sampling rate of the respiratory belt was 500 Hz. Frequency of each breath was calculated and compared between the respiration belt and our optical system. The respiration frequency detected by the structured light system and the respiratory belt were compared using t-test and intraclass correlation coefficient (ICC). 95% confidence intervals were calculated (R, v3.0.2).

4.6.3 *Results*

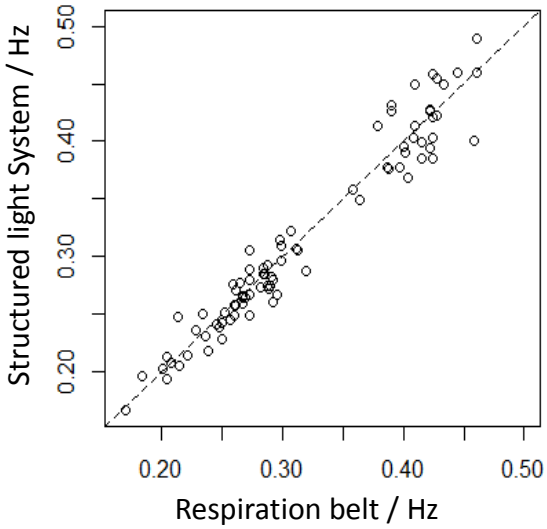

Figure 4-11. Respiration frequency detected using structured light system highly correlated with that detected using breathing belt.

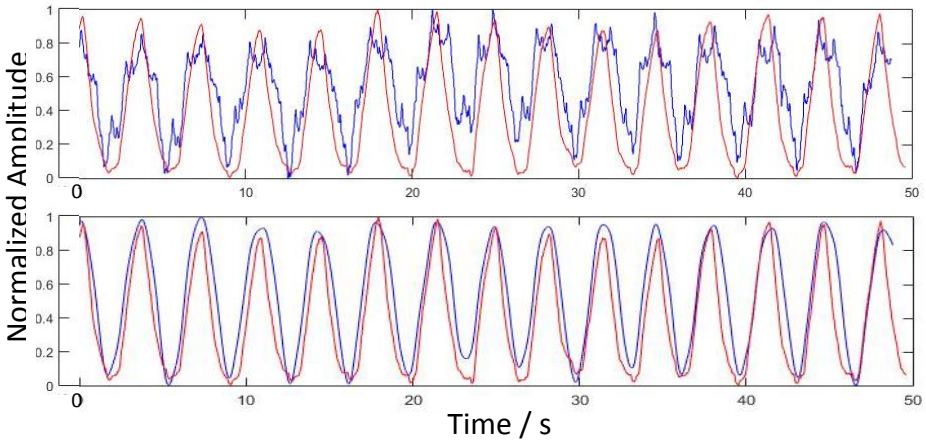

Figure 4-12. Comparison between respirations detected using our structured light system (blue curve) and breathing belt (red curve). The top image shows the raw motion record and the bottom image shows the filtered motion record.

On average, 17 $\pm$ 4 breaths were measured per subject. After bandpass filtering, the respiration motion detected using the structured light system correlated well with that detected using the respiratory belt (Figure 4-11). One volunteer example was shown in Figure 4-12. There was no

significant difference between the respiration frequency measured by the structured light system and that measured by the respiration belt (0.321 ± 0.077 Hz and 0.320 ± 0.078 Hz, respectively) with a p-value of 0.866. The ICC of respiration frequency was 0.97 (0.95, 0.98).

4.6.4 *Discussion*

The non-marker-attached structured light motion detection system has been demonstrated previously to be able to detect and correct abrupt motion (e.g. cough and swallowing) and bulk shift motion, by projecting a laser light onto the neck of the subject. Therefore, using a structured light system is promising as an integrated motion detection solution, with both physiological motion and voluntary motion detected simultaneously.

One limitation of this study was that the sample size was relatively small. More volunteers and patients are needed to prove the robustness of this respiration motion detection efficiency. In addition, the respiration motion extraction in this study was performed retrospectively. Real-time filter need to be developed for prospective respiration tracking if breathing gating is needed.

4.6.5 *Summary*

It was demonstrated that a non-marker-attached structured light system can detect respiration motion. The accuracy of respiration frequency was highly correlated with that detected by the respiration belt.

Chapter 5. CONCLUSION AND FUTURE DIRECTIONS

5.1 SIGNIFICANT CONTRIBUTIONS

This work demonstrated the first attempt to obtain histology-validated criteria for intraplaque hemorrhage detection and quantification. The previous automatic intraplaque hemorrhage detection studies all utilized arbitrary thresholds for intraplaque hemorrhage detection. In this study, multiple MR signal intensity normalization methods were proposed and compared in MP-RAGE sequence. It was demonstrated that in the widely used MP-RAGE MR images, using adjacent soft tissue as the reference had good intraplaque hemorrhage detection performance yet a big sternocleidomastoid muscle area did not qualify for a good normalization reference due to its vicinity to the surface coil. Note that median value had similar performance with the adjacent soft tissue and has the intrinsic advantage of allowing for more automatic detection. However, in SNAP sequence where coil inhomogeneity was already corrected and the above references had close-to-zero intensity, sternocleidomastoid muscle in the SNAP reference image can be used for intensity normalization.

The time-efficient intraplaque hemorrhage quantification method based on 3D SNAP MR was developed and high scan-rescan reproducibility of both intraplaque hemorrhage volume and intensity were demonstrated. Importantly, the rescanned data within one month also showed a trend of decreasing intraplaque hemorrhage volume, which may indicate intraplaque hemorrhage quantification matrix as a much rapid changing progress compared with intraplaque hemorrhage presence and warrant further study.

The novel motion detection and correction on MRI based on structured light was developed and good detection and correction effect for both abrupt motion (like swallowing and cough) and bulk motion on carotid MRI was demonstrated. None of previous carotid MRI motion correction methods have been demonstrated the ability of correcting for bulk motion, which is a frequent problem especially when there is abrupt motion. Respiration motion was also detected and validated using this sensitive optical motion detection system. Furthermore, this proposed method has the intrinsic merit of MR sequence independency and is non-attached to the patient.

5.2 Future Directions

This dissertation has provided a semi-automatic and reproducible intraplaque hemorrhage quantification method with intraplaque hemorrhage detection criteria validated based on histology. Using this method, it would be feasible to monitor intraplaque hemorrhage progression in longitudinal studies to investigate intraplaque hemorrhage quantitative signal change and its relationship with atherosclerosis progression.

As demonstrated in the previous chapter, the proposed motion detection and correction system using structured light has achieved improved vessel wall delineation in healthy volunteer carotid MR scans. Next, this technique can be validated on intraplaque hemorrhage detection to access its clinical usage. By recruiting carotid atherosclerosis patients, especially patients scheduled for carotid endarterectomy, the hypothesis that motion correction for carotid MRI can improve intraplaque hemorrhage detection sensitivity and quantification accuracy, as well as other carotid plaque components delineation, can be tested.

Technical improvements for the proposed motion detection and correction system could also be done in the future. 1) One direction is to perform prospective motion correction. If motion is detected, instruction will be transmitted to the MR scanner to rescan the corrupted k-space lines. The technical challenge for prospective motion correction is the communication interface with MR scanner and manipulating scan process. 2) Another improvement would be motion correction in 3D MRI, such as SNAP sequence. The modification should be straightforward, because for both abrupt motion and bulk motion, the proposed motion correction method could be applied to 3D images and k-spaces, respectively. 3) Also, using the detected respiration motion information, it would be feasible to correct for respiration motion [86] in both carotid MRI and MRI in other areas such as abdomen. It was reported that breathing could cause carotid artery motion of around 1.56 ± 0.99 mm [50]. Considering that the thickness of healthy carotid vessel wall is only around 0.5 mm, breathing could impact the visualization of carotid artery, especially for patients with heavy breathing. 4) A more complex laser pattern, such as a grid, multiple parallel lines or random pattern, could be used to record more motion information. In this way, the whole surface height within laser pattern area could be captured, which may give more accurate motion information.

Lastly, although the proposed motion detection and correction has been mainly focused on carotid MRI, this technique is certainly applicable to other areas for both rigid and non-rigid motion correction, as long as motion can be detected on the surface of the object.

BIBLIOGRAPHY

1. Lozano, R., et al., *Global and regional mortality from 235 causes of death for 20 age groups in 1990 and 2010: a systematic analysis for the Global Burden of Disease Study 2010.* Lancet, 2012. **380**(9859): p. 2095-128.

2. Go, A.S., et al., *Heart disease and stroke statistics--2014 update: a report from the american heart association.* Circulation, 2014. **129**(3): p. e28-e292.

3. Nichols, M., et al., *Cardiovascular disease in Europe 2014: epidemiological update.* Eur Heart J, 2014. **35**(42): p. 2929.

4. Naghavi, M., et al., *From vulnerable plaque to vulnerable patient: a call for new definitions and risk assessment strategies: Part I.* Circulation, 2003. **108**(14): p. 1664-72.

5. Ross, R., *Atherosclerosis--an inflammatory disease.* N Engl J Med, 1999. **340**(2): p. 115-26.

6. Sadeghi, M.M., et al., *Imaging atherosclerosis and vulnerable plaque.* J Nucl Med, 2010. **51 Suppl 1**: p. 51S-65S.

7. Ambrose, J.A., et al., *Angiographic progression of coronary artery disease and the development of myocardial infarction.* J Am Coll Cardiol, 1988. **12**(1): p. 56-62.

8. McCarthy, M.J., et al., *Angiogenesis and the atherosclerotic carotid plaque: An association between symptomatology and plaque morphology.* Journal of Vascular Surgery, 1999. **30**(2): p. 261-268.

9. Figueroa, A.L., et al., *Distribution of Inflammation Within Carotid Atherosclerotic Plaques With High-Risk Morphological Features A Comparison Between Positron Emission Tomography Activity, Plaque Morphology, and Histopathology.* Circulation-Cardiovascular Imaging, 2012. **5**(1): p. 69-77.

10. Virmani, R., et al., *Atherosclerotic plaque progression and vulnerability to rupture: angiogenesis as a source of intraplaque hemorrhage.* Arterioscler Thromb Vasc Biol, 2005. **25**(10): p. 2054-61.

11. Milei, J., et al., *Carotid rupture and intraplaque hemorrhage: immunophenotype and role of cells involved.* Am Heart J, 1998. **136**(6): p. 1096-105.

12. Michel, J.B., et al., *Intraplaque haemorrhages as the trigger of plaque vulnerability.* European Heart Journal, 2011. **32**(16): p. 1977-U46.

13. Takaya, N., et al., *Presence of intraplaque hemorrhage stimulates progression of carotid atherosclerotic plaques - A high-resolution magnetic resonance Imaging study.* Circulation, 2005. **111**(21): p. 2768-2775.

14. Takaya, N., et al., *Association between carotid plaque characteristics and subsequent ischemic cerebrovascular events - A prospective assessment with MRI - Initial results.* Stroke, 2006. **37**(3): p. 818-823.

15. Singh, N., et al., *Moderate carotid artery stenosis: MR imaging-depicted intraplaque hemorrhage predicts risk of cerebrovascular ischemic events in asymptomatic men.* Radiology, 2009. **252**(2): p. 502-8.

16. Kolodgie, F.D., et al., *Intraplaque hemorrhage and progression of coronary atheroma.* N Engl J Med, 2003. **349**(24): p. 2316-25.

17. Altaf, N., et al., *Detection of intraplaque hemorrhage by magnetic resonance imaging in symptomatic patients with mild to moderate carotid stenosis predicts recurrent neurological events.* J Vasc Surg, 2008. **47**(2): p. 337-42.

18. Lin, R., et al., *Association Between Carotid Atherosclerotic Plaque Calcification and Intraplaque HemorrhageHighlights.* Arteriosclerosis, Thrombosis, and Vascular Biology, 2017. **37**(6): p. 1228-1233.

19. Wintermark, M., et al., *High-resolution CT imaging of carotid artery atherosclerotic plaques.* AJNR Am J Neuroradiol, 2008. **29**(5): p. 875-82.

20. Kidwell, C.S. and M. Wintermark, *Imaging of intracranial haemorrhage.* Lancet Neurol, 2008. **7**(3): p. 256-67.

21. Widder, B., et al., *Morphological characterization of carotid artery stenoses by ultrasound duplex scanning.* Ultrasound Med Biol, 1990. **16**(4): p. 349-54.

22. Liu, J., et al., *High resolution FDG-microPET of carotid atherosclerosis: plaque components underlying enhanced FDG uptake.* Int J Cardiovasc Imaging, 2016. **32**(1): p. 145-52.

23. Bradley, W.G., Jr., *MR appearance of hemorrhage in the brain.* Radiology, 1993. **189**(1): p. 15-26.

24. Moody, A.R., et al., *Characterization of complicated carotid plaque with magnetic resonance direct thrombus imaging in patients with cerebral ischemia.* Circulation, 2003. **107**(24): p. 3047-52.

25. Zhu, D.C., M.S. Ferguson, and J.K. DeMarco, *An optimized 3D inversion recovery prepared fast spoiled gradient recalled sequence for carotid plaque hemorrhage imaging at 3.0 T.* Magn Reson Imaging, 2008. **26**(10): p. 1360-6.

26. Yuan, C., et al., *In vivo accuracy of multispectral magnetic resonance imaging for identifying lipid-rich necrotic cores and intraplaque hemorrhage in advanced human carotid plaques.* Circulation, 2001. **104**(17): p. 2051-6.

27. Mugler, J.P., 3rd and J.R. Brookeman, *Three-dimensional magnetization-prepared rapid gradient-echo imaging (3D MP RAGE).* Magn Reson Med, 1990. **15**(1): p. 152-7.

28. Moody, A.R., et al., *Characterization of complicated carotid plaque with magnetic resonance direct thrombus imaging in patients with cerebral ischemia.* Circulation, 2003. **107**(24): p. 3047-3052.

29. Chu, B., et al., *Hemorrhage in the atherosclerotic carotid plaque: a high-resolution MRI study.* Stroke, 2004. **35**(5): p. 1079-84.

30. Ota, H., et al., *Carotid Intraplaque Hemorrhage Imaging at 3.0-T MR Imaging: Comparison of the Diagnostic Performance of Three T1-weighted Sequences.* Radiology, 2010. **254**(2): p. 551-563.

31. Bitar, R., et al., *In vivo 3D high-spatial-resolution MR imaging of intraplaque hemorrhage.* Radiology, 2008. **249**(1): p. 259-67.

32. Wang, J., et al., *Simultaneous noncontrast angiography and intraplaque hemorrhage (SNAP) imaging for carotid atherosclerotic disease evaluation.* Magn Reson Med, 2013. **69**(2): p. 337-45.

33. Hishikawa, T., et al., *Assessment of necrotic core with intraplaque hemorrhage in atherosclerotic carotid artery plaque by MR imaging with 3D gradient-echo sequence in patients with high-grade stenosis. Clinical article.* J Neurosurg, 2010. **113**(4): p. 890-6.

34. Liu, J., et al., *Semi-automatic carotid intraplaque hemorrhage detection and quantification on Magnetization-Prepared Rapid Acquisition Gradient-Echo (MP-RAGE) with optimized threshold selection.* Journal of Cardiovascular Magnetic Resonance, 2016. **18**.

35. Shah, M., et al., *Evaluating intensity normalization on MRIs of human brain with multiple sclerosis.* Med Image Anal, 2011. **15**(2): p. 267-82.

36. Yamada, N., et al., *Association between signal hyperintensity on T1-weighted MR imaging of carotid plaques and ipsilateral ischemic events.* American Journal of Neuroradiology, 2007. **28**(2): p. 287-292.

37. Mendes, J., et al., *Reduced blood flow artifact in intraplaque hemorrhage imaging using CineMPRAGE.* Magn Reson Med, 2013. **69**(5): p. 1276-84.

38. Simpson, R.J., et al., *MR Imaging-Detected Carotid Plaque Hemorrhage Is Stable for 2 Years and a Marker for Stenosis Progression.* American Journal of Neuroradiology, 2015. **36**(6): p. 1171-1175.

39. Wang, Q.J., et al., *Differences of signal evolution of intraplaque hemorrhage and associated stenosis between symptomatic and asymptomatic atherosclerotic carotid arteries: an in vivo high-resolution magnetic resonance imaging follow-up study.* International Journal of Cardiovascular Imaging, 2010. **26**: p. 323-332.

40. van den Bouwhuijsen, Q.J., et al., *Change in Carotid Intraplaque Hemorrhage in Community-dwelling Subjects: A Follow-up Study Using Serial MR Imaging.* Radiology, 2016: p. 151806.

41. Wang, X., et al., *Ipsilateral plaques display higher T1 signals than contralateral plaques in recently symptomatic patients with bilateral carotid intraplaque hemorrhage.* Atherosclerosis, 2017. **257**: p. 78-85.

42. Sun, J., et al., *Blood Pressure Is a Major Modifiable Risk Factor Implicated in Pathogenesis of Intraplaque Hemorrhage An In Vivo Magnetic Resonance Imaging Study.* Arteriosclerosis Thrombosis and Vascular Biology, 2016. **36**(4): p. 743-749.

43. Hosseini, A.A., et al., *Carotid plaque hemorrhage on magnetic resonance imaging strongly predicts recurrent ischemia and stroke.* Ann Neurol, 2013. **73**(6): p. 774-84.

44. Li, F., et al., *Scan-rescan reproducibility of carotid atherosclerotic plaque morphology and tissue composition measurements using multicontrast MRI at 3T.* J Magn Reson Imaging, 2010. **31**(1): p. 168-76.

45. Wasserman, B.A., et al., *MRI Measurements of Carotid Plaque in the Atherosclerosis Risk in Communities (ARIC) Study: Methods, Reliability and Descriptive Statistics.* Journal of Magnetic Resonance Imaging, 2010. **31**(2): p. 406-415.

46. Sun, J., et al., *Carotid magnetic resonance imaging for monitoring atherosclerotic plaque progression: a multicenter reproducibility study.* International Journal of Cardiovascular Imaging, 2015. **31**(1): p. 95-103.

47. Boussel, L., et al., *Atherosclerotic plaque progression in carotid arteries: monitoring with high-spatial-resolution MR imaging--multicenter trial.* Radiology, 2009. **252**(3): p. 789-96.

48. Andre, J.B., et al., *Toward Quantifying the Prevalence, Severity, and Cost Associated With Patient Motion During Clinical MR Examinations.* J Am Coll Radiol, 2015. **12**(7): p. 689-95.

49. Hedley, M. and H. Yan, *Motion artifact suppression: a review of post-processing techniques.* Magn Reson Imaging, 1992. **10**(4): p. 627-35.

50. Boussel, L., et al., *Swallowing, arterial pulsation, and breathing induce motion artifacts in carotid artery MRI.* J Magn Reson Imaging, 2006. **23**(3): p. 413-5.

51. Pauletto, P., et al., *Factors underlying the increase in carotid intima-media thickness in borderline hypertensives.* Arterioscler Thromb Vasc Biol, 1999. **19**(5): p. 1231-7.

52. Maclaren, J., et al., *Prospective motion correction in brain imaging: a review.* Magn Reson Med, 2013. **69**(3): p. 621-36.

53. Koktzoglou, I. and D. Li, *Submillimeter isotropic resolution carotid wall MRI with swallowing compensation: imaging results and semiautomated wall morphometry.* J Magn Reson Imaging, 2007. **25**(4): p. 815-23.

54. Crowe, L.A., et al., *3D volume-selective turbo spin echo for carotid artery wall imaging with navigator detection of swallowing.* J Magn Reson Imaging, 2005. **22**(4): p. 583-8.

55. Dyverfeldt, P., et al., *Reduction of motion artifacts in carotid MRI using free-induction decay navigators.* J Magn Reson Imaging, 2014. **40**(1): p. 214-20.

56. Fan, Z., et al., *Prospective self-gating for swallowing motion: a feasibility study in carotid artery wall MRI using three-dimensional variable-flip-angle turbo spin-echo.* Magn Reson Med, 2012. **67**(2): p. 490-8.

57. Chan, C.F., et al., *Novel Technique Used to Detect Swallowing in Volume-Selective Turbo Spin-Echo (TSE) for Carotid Artery Wall Imaging.* Journal of Magnetic Resonance Imaging, 2009. **29**(1): p. 211-216.

58. Jason K Mendes, D.L.P., Robb Merrill, J Rock Hadley. *A Novel Swallow Detection Device For Carotid Artery Imaging*. in *21st ISMRM*. 2013. Salt lake city, Utah, USA.

59. Taylor, A.M., et al., *Automated monitoring of diaphragm end-expiratory position for real-time navigator echo MR coronary angiography.* J Magn Reson Imaging, 1999. **9**(3): p. 395-401.

60. Huang, F., et al., *Data convolution and combination operation (COCOA) for motion ghost artifacts reduction.* Magn Reson Med, 2010. **64**(1): p. 157-66.

61. Chen, H.J., J. Zhang, and J. Fang, *Surface height retrieval based on fringe shifting of color-encoded structured light pattern.* Opt Lett, 2008. **33**(16): p. 1801-3.

62. Olesen, O.V., et al., *Motion tracking for medical imaging: a nonvisible structured light tracking approach.* IEEE Trans Med Imaging, 2012. **31**(1): p. 79-87.

63. Erikshoj, M., et al., *Structured light-based motion tracking in the limited view of an MR head coil.* Nuclear Instruments & Methods in Physics Research Section a-Accelerators Spectrometers Detectors and Associated Equipment, 2013. **702**: p. 117-120.

64. Cai, J., et al., *In vivo quantitative measurement of intact fibrous cap and lipid-rich necrotic core size in atherosclerotic carotid plaque: comparison of high-resolution, contrast-enhanced magnetic resonance imaging and histology.* Circulation, 2005. **112**(22): p. 3437-44.

65. Saam, T., et al., *Quantitative evaluation of carotid plaque composition by in vivo MRI.* Arterioscler Thromb Vasc Biol, 2005. **25**(1): p. 234-9.

66. Saam, T., et al., *Comparison of symptomatic and asymptomatic atherosclerotic carotid plaque features with in vivo MR imaging.* Radiology, 2006. **240**(2): p. 464-72.

67. Liu, F., et al., *Automated in vivo segmentation of carotid plaque MRI with morphology-enhanced probability maps.* Magnetic Resonance in Medicine, 2006. **55**(3): p. 659-668.

68. Han, C., T.S. Hatsukami, and C. Yuan, *A multi-scale method for automatic correction of intensity non-uniformity in MR images.* J Magn Reson Imaging, 2001. **13**(3): p. 428-36.

69. Kellman, P., et al., *Phase-sensitive inversion recovery for detecting myocardial infarction using gadolinium-delayed hyperenhancement.* Magnetic Resonance in Medicine, 2002. **47**(2): p. 372-383.

70. Shu, H., et al., *Simultaneous noncontrast angiography and intraplaque hemorrhage (SNAP) imaging: Comparison with contrast-enhanced MR angiography for measuring carotid stenosis.* J Magn Reson Imaging, 2017.

71. Davison, A.C. and D.V. Hinkley, *Bootstrap methods and their application*. 1997, Cambridge, UK ; New York, NY, USA: Cambridge University Press. x, 582 p.

72. Team, R.C., *R: A language and environment for statistical computing.* 2012.

73. Balu, N., et al., *Improvements in Carotid Plaque Imaging Using a New Eight-Element Phased Array Coil at 3T.* Journal of Magnetic Resonance Imaging, 2009. **30**(5): p. 1209-1214.

74. Levy, P., *The Design and Analysis of Clinical Experiments - Fleiss,Jl.* British Journal of Mathematical & Statistical Psychology, 1987. **40**: p. 98-99.

75. Landis, J.R. and G.G. Koch, *The measurement of observer agreement for categorical data.* Biometrics, 1977. **33**(1): p. 159-74.

76. Zhou, C., et al., *Characterization of atherosclerotic disease in thoracic aorta: A 3D, multicontrast vessel wall imaging study.* Eur J Radiol, 2016. **85**(11): p. 2030-2035.

77. Wang, J., et al., *In Vivo Validation of Simultaneous Non-Contrast Angiography and intraPlaque Hemorrhage (SNAP) Magnetic Resonance Angiography: An Intracranial Artery Study.* PLoS One, 2016. **11**(2): p. e0149130.

78. Noguchi, T., et al., *Effect of Intensive Statin Therapy on Coronary High-Intensity Plaques Detected by Noncontrast T1-Weighted Imaging The AQUAMARINE Pilot Study.* Journal of the American College of Cardiology, 2015. **66**(3): p. 245-256.

79. Touze, E., et al., *Reproducibility of high-resolution MRI for the identification and the quantification of carotid atherosclerotic plaque components consequences for prognosis studies and therapeutic trials.* Stroke, 2007. **38**(6): p. 1812-1819.

80. Tang, H., et al., *Semi-automatic MRI segmentation and volume quantification of intra-plaque hemorrhage.* International Journal of Computer Assisted Radiology and Surgery, 2015. **10**(1): p. 67-74.

81. Chen, H., et al., *Color structured light system of chest wall motion measurement for respiratory volume evaluation.* J Biomed Opt, 2010. **15**(2): p. 026013.

82. Canny, J., *A computational approach to edge detection.* IEEE Trans Pattern Anal Mach Intell, 1986. **8**(6): p. 679-98.

83. Lustig, M. and J.M. Pauly, *SPIRiT: Iterative self-consistent parallel imaging reconstruction from arbitrary k-space.* Magn Reson Med, 2010. **64**(2): p. 457-71.

84. Griswold, M.A., et al., *Generalized autocalibrating partially parallel acquisitions (GRAPPA).* Magn Reson Med, 2002. **47**(6): p. 1202-10.

85. Mills, D.L., *Computer Network Time Synchronization: The Network Time Protocol*. 2006: CRC Press.

86. Pang, J., et al., *Whole-heart coronary MRA with 100% respiratory gating efficiency: self-navigated three-dimensional retrospective image-based motion correction (TRIM).* Magn Reson Med, 2014. **71**(1): p. 67-74.

VITA

Jin Liu obtained her Bachelor degree on Biomedical Engineering from Tianjin University, Tianjin, China. She then moved to Seattle and continued her graduate study in the Department of Bioengineering, University of Washington. As a graduate student and research assistant, her research has been focuses on carotid intraplaque hemorrhage detection and quantification on MRI, as well as developing motion detection and correction method for MRI using structured light-based optical system.